Quaternary Science Reviews 175 (2017) 112–137

Contents lists available at ScienceDirect

Quaternary Science Reviews

journal homepage: www.elsevier.com/locate/quascirev

Subduction zone slip variability during the last millennium, south-central Chile☆

Tina Dura [a, *], Benjamin P. Horton [a, b, c], Marco Cisternas [d], Lisa L. Ely [e], Isabel Hong [a], Alan R. Nelson [f], Robert L. Wesson [e], Jessica E. Pilarczyk [g], Andrew C. Parnell [h], Daria Nikitina [i]

[a] Sea Level Research, Department of Marine and Coastal Science, Rutgers University, New Brunswick, NJ, USA
[b] Asian School of the Environment, Nanyang Technological University, Singapore
[c] Earth Observatory of Singapore, Nanyang Technological University, Singapore
[d] Escuela de Ciencias del Mar, Pontificia Universidad Católica de Valparaíso, Valparaíso, Chile
[e] Department of Geological Sciences, Central Washington University, Ellensburg, WA, USA
[f] Geologic Hazards Science Center, U.S. Geological Survey, Golden, CO, USA
[g] Division of Marine Science, School of Ocean Science and Technology, University of Southern Mississippi, Stennis Space Center, MS, USA
[h] School of Mathematical Sciences, Insight Centre for Data Analytics, University College Dublin, Ireland
[i] Department of Earth and Space Sciences, West Chester University, West Chester, PA, USA

ARTICLE INFO

Article history:
Received 25 April 2017
Received in revised form
22 July 2017
Accepted 25 August 2017
Available online 19 October 2017

Keywords:
Prehistoric earthquakes
Subduction zone segmentation
Tsunami deposits
Diatom paleoecology
Coastal paleoseismology
Coastal hazards

ABSTRACT

The Arauco Peninsula (37°-38°S) in south-central Chile has been proposed as a possible barrier to the along-strike propagation of megathrust ruptures, separating historical earthquakes to the south (1960 AD 1837, 1737, and 1575) and north (2010 AD, 1835, 1751, 1657, and 1570) of the peninsula. However, the 2010 (M_w 8.8) earthquake propagated into the Arauco Peninsula, re-rupturing part of the megathrust that had ruptured only 50 years earlier during the largest subduction zone earthquake in the instrumental record (M_w 9.5). To better understand long-term slip variability in the Arauco Peninsula region, we analyzed four coastal sedimentary sections from two sites (Tirúa, 38.3°S and Quidico, 38.1°S) located within the overlap of the 2010 and 1960 ruptures to reconstruct a ~600-year record of coseismic land-level change and tsunami inundation. Stratigraphic, lithologic, and diatom results show variable coseismic land-level change coincident with tsunami inundation of the Tirúa and Quidico marshes that is consistent with regional historical accounts of coseismic subsidence during earthquakes along the Valdivia portion of the subduction zone (1960 AD and 1575) and coseismic uplift during earthquakes along the Maule portion of the subduction zone (2010 AD, 1835, 1751). In addition, we document variable coseismic land-level change associated with three new prehistoric earthquakes and accompanying tsunamis in 1470–1570 AD, 1425–1455, and 270–410. The mixed record of coseismic subsidence and uplift that we document illustrates the variability of down-dip and lateral slip distribution at the overlap of the 2010 and 1960 ruptures, showing that ruptures have repeatedly propagated into, but not through the Arauco Peninsula and suggesting the area has persisted as a long-term impediment to slip through at least seven of the last megathrust earthquakes (~600 years).

1. Introduction

Subduction zone paleogeodesy, which combines the methods of coastal stratigraphy, micropaleontology, and geophysical modeling to reconstruct coseismic and interseismic land-level change (e.g., Witter et al., 2003; Briggs et al., 2014; Shennan et al., 2016), is critical to understanding the magnitude, frequency, and spatial extent of ruptures over multiple earthquake cycles along the south-central Chilean subduction zone (35°-43°S). Although the region

☆ Peer Review DISCLAIMER: This draft manuscript is distributed solely for purposes of scientific peer review. Its content is deliberative and predecisional, so it must not be disclosed or released by reviewers. Because the manuscript has not yet been approved for publication by the U.S. Geological Survey (USGS), it does not represent any official USGS finding or policy.

* Corresponding author. Sea Level Research, Department of Marine and Coastal Science, Rutgers University, 71 Dudley Rd., New Brunswick 08901, NJ, USA.
E-mail address: dura@marine.rutgers.edu (T. Dura).

https://doi.org/10.1016/j.quascirev.2017.08.023
0277-3791/

benefits from a 500-year historical record of earthquakes and tsunamis (Lomnitz, 1970; Cisternas et al., 2005, 2012, 2017b; Udias et al., 2012), written accounts and stratigraphic records of coseismic land-level changes and tsunami inundation are geographically limited, resulting in poorly constrained rupture extents even for recent historical events (Plafker and Savage, 1970; Lomnitz, 2004; Moreno et al., 2012). As a result, the causes of slip heterogeneity during great earthquakes in south-central Chile are not well understood (Lay, 2011; Lorito et al., 2011; Moreno et al., 2011).

A good example is the proposed megathrust rupture boundary at the Arauco Peninsula (37°-38°S; Fig. 1; Rehak et al., 2008). Historical accounts indicate that ruptures in south-central Chile were mostly confined to either the Valdivia portion of the subduction zone south of the Arauco Peninsula (1960 AD, 1837, 1737, and 1575), or the Maule portion of the subduction zone north of the Arauco Peninsula (2010 AD, 1835, 1751, 1657, and 1570) (Lomnitz, 1970; Cisternas et al., 2005, 2012, 2017b; Udias et al., 2012). However, the 2010 (M_w 8.8) Maule rupture overlapped with the northern ~90 km of the 1960 (M_w 9.5) rupture across the Arauco Peninsula (Fig. 1b), highlighting the complexity of slip in this region and calling into question the persistence of the proposed megathrust rupture boundary.

Here we apply subduction zone paleogeodesy at two estuaries (Tirúa, 38.3°S and Quidico, 38.1°S) located within the overlap of the 2010 and 1960 earthquakes in order to explore coseismic slip variability over many centuries and, in particular, to test the persistence of the proposed megathrust rupture boundary (Fig. 1; Melnick et al., 2009; Moreno et al., 2011). We expand upon previous

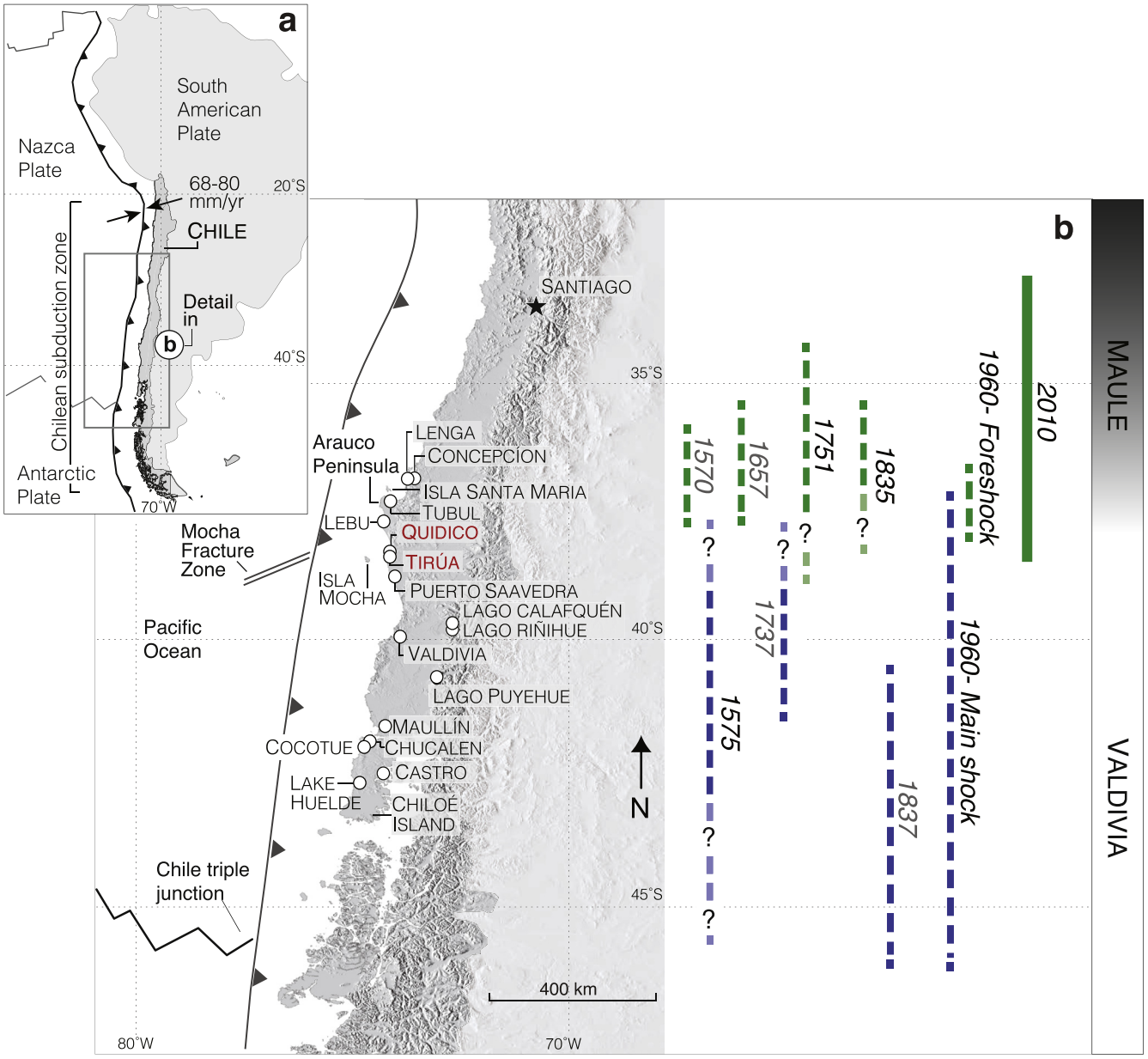

Fig. 1. Index maps. a) Plate-tectonic setting of Chile in western South America. b) Location of the study area in central Chile, the Valdivia and Maule portions of the subduction zone, main tectonic features, and rupture lengths of the largest historical earthquakes in south-central Chile since 1570 shown by dashed lines where inferred and solid lines where measured. Green lines denote earthquakes associated with the Maule portion of the subduction zone and blue lines denote earthquakes associated with the Valdivia portion of the subduction zone. Inferred and approximated rupture extents compiled from Barrientos (2007), (1970), Kelleher (1972), Beck et al. (1998), Melnick et al. (2009), Udías et al. (2012), Melnick et al. (2012), and Cisternas et al. (2017b). (For interpretation of the references to colour in this figure legend, the reader is referred to the web version of this article.)

studies at the same sites by Ely et al. (2014) and Hong et al. (2017) that identified stratigraphic evidence of four historical tsunamis at Tirúa and four historical and one prehistoric tsunami at Quidico. We apply additional stratigraphic, sedimentologic, and diatom analyses to reconstruct coseismic land-level change coincident with previously documented tsunamis, strengthen the interpreted correlations of tsunami sand layers between these sites, and to identify two new prehistoric tsunamis. Our new land-level change reconstructions show that historical and prehistoric ruptures along the Valdivia and Maule portions of the subduction zone have repeatedly propagated into and overlapped within the Arauco Peninsula, resulting in complex slip patterns that are influenced by the southern or northern genesis of the ruptures.

2. Approach

2.1. Subduction zone paleogeodesy

In parallel with new appreciation for the variability of coseismic and interseismic deformation at subduction zones, including patterns of down-dip and lateral slip distribution during great (M8-9) megathrust earthquakes demonstrated by recent field geodetic surveys, continuous GPS measurements, and increasingly sophisticated modeling, has come recognition of the need for documenting subduction zone deformation over multiple great earthquake cycles (e.g., Thatcher, 1990; Dragert et al., 2001; Pollitz et al., 2006; Simons et al., 2011; Vigny et al., 2011; Moreno et al., 2012; Wang et al., 2013). Reconstructing the coastal land-level changes that record deformation over the many centuries spanned by such cycles requires the application of paleogeodesy (e.g., Shennan and Hamilton, 2006; Satake and Atwater, 2007; Sieh et al., 2008; Bilek, 2010; Meltzner et al., 2012; Witter et al., 2014; Wesson et al., 2015; Melnick et al., 2017).

Subduction zone paleogeodetic studies document the paleoenvironmental changes caused by sudden (coseismic) relative sea level (RSL) rises or falls during great earthquakes. Sudden RSL rises or falls are expressed in coastal sedimentary sequences as distinctive changes in sediment lithology across sharp stratigraphic contacts, often accompanied by abrupt changes in microfossil assemblages (Atwater and Hemphill-Haley, 1997; Hamilton and Shennan, 2005; Hawkes et al., 2011; Horton et al., 2017). Sand beds that accompany stratigraphic evidence of sudden RSL change often contain allochthonous microfossils that indicate deposition by tsunamis accompanying great earthquakes (Hemphill-Haley, 1996; Sawai, 2001; Sawai et al., 2012; Pilarczyk et al., 2014; Dura et al., 2016a). Subsequent gradual changes in sediment lithology and microfossil assemblages above sharp stratigraphic contacts or tsunami deposits then typically record gradual RSL change during the interseismic component of the earthquake deformation cycle (Sawai et al., 2004; Shennan et al., 2014; Dura et al., 2015). Measurement of amounts and rates of coseismic and interseismic land-level change preserved within sedimentary sequences can constrain elastic dislocation models used to reconstruct slip distributions over megathrust surfaces during past subduction zone earthquakes (Wang et al., 2003, 2013).

2.2. Selection of study sites

In south-central Chile, the Nazca plate subducts to the northeast at an angle of ~15° beneath the South American plate at ~66 mm/yr (Angermann et al., 1999). Within this region, the Arauco Peninsula, which is a ~100 km-wide zone of crustal upwarping and high uplift rates bounded by the tip of the Peninsula (~37°S) and the Lanalhue fault (~38°S), separates the highly coupled Maule portion of the subduction zone to the north and the Valdivia portion of the subduction zone to the south (Fig. 1b; Rehak et al., 2008; Métois et al., 2012; Jara-Munoz et al., 2015). Changes in the curvature of the megathrust and frictional properties at the Arauco Peninsula have been proposed as a barrier to the along-strike propagation of ruptures; however, the 2010 and 1960 earthquakes (and possibly earthquakes in 1835 AD, 1751, and 1575) overlapped within this broad zone of crustal upwarping (Jara-Munoz et al., 2015).

Our study sites at Tirúa (38.3°S) and Quidico (38.1°S) are located ~30 km south of the Lanalhue fault, within the overlap of the 2010 and 1960 ruptures (Fig. 1). Historical accounts and geologic evidence associated with ruptures on the Valdivia portion of the subduction zone (e.g., 1960 AD, 1575) show coseismic subsidence at sites south of Tirúa and Quidico, while historical accounts and geologic evidence associated with ruptures on the Maule portion of the subduction zone (e.g., 2010 AD, 1835, 1751) show coseismic uplift at sites north of Tirúa and Quidico (Fig. 1b; e.g., de Moralda, 1780s; Lomnitz, 1970; Plafker and Savage, 1970; Cisternas et al., 2005; Udías et al., 2012; Melnick et al., 2012; and Cisternas et al., 2017b). However, historical accounts and geologic evidence of coseismic land-level change in the immediate Tirúa and Quidico area only exist for the 2010 AD and 1960 ruptures (Plafker and Savage, 1970; Farías et al., 2010; Melnick et al., 2012; Ely et al., 2014), leaving the slip distribution of past ruptures in the overlap of the 2010 and 1960 ruptures poorly resolved.

The low-energy tidal marshes, coastal plains, and abandoned meanders bordering the tidal Tirúa and Quidico Rivers are covered with freshwater to brackish marsh plant communities (e.g., *Juncus balticus, Juncus microcephalus, Schoenoplectus americanus, Schoenoplectus californicus,* and *Spartina* sp.), which provide favorable environments for preservation of stratigraphic evidence of sudden RSL rises or falls during past subduction zone earthquakes. A RSL fall from abrupt coseismic uplift would result in a decrease in tidal inundation in marshes bordering the rivers, reflected by an increase in saline-intolerant plants and freshwater diatoms. A RSL rise during sudden coseismic subsidence would result in an increase in tidal inundation, which would be reflected by an increase in salt-tolerant plants and marine and brackish diatoms.

2.3. Previous work at Tirúa and Quidico

Previous studies at Tirúa (Ely et al., 2014) and Quidico (Hong et al., 2017) employed geomorphic, sedimentological, and stratigraphic methods to interpret sequences of laterally extensive (>300 m) sand beds interbedded within organic-rich silts and sands as evidence for repeated late Holocene tsunami inundation (Fig. 3). Four sand beds described at Tirúa and five sand beds described at Quidico are composed of well-sorted, anomalously coarse sediment with a low organic content and display uniform thickness and sharp (1–3 mm) lower and upper contacts (Fig. 3). The authors used the lithology, lateral continuity, and tabular geometry of the sand beds to help rule out localized processes, such as tidal channel migration, liquefaction, or sand venting during earthquakes as sources for sand bed deposition (Fig. 3; e.g., Atwater et al., 1992; Allen, 2000; Cisternas et al., 2005; Goto et al., 2011; Szczuciński et al., 2012). Ely et al. (2014) and Hong et al. (2017) used detailed radiocarbon, optically stimulated luminescence (OSL), and ^{137}Cs analyses combined with historical accounts of earthquake shaking and tsunami inundation to develop chronologies for the sand bed sequences).

^{137}Cs analysis and witnesses at Tirúa and Quidico that described inundation of the sites following the 1960 AD and 2010 earthquakes, support a tsunami origin for the two youngest sand beds (sand beds 1 and 2 in this study). Based on the modeled age range of the third oldest sand bed (sand bed 3 in this study) at Quidico (1660–1959 AD) and the historical rupture extents of past

earthquakes, Hong et al. (2017) eliminated the 1837 AD (too far south) and 1730 AD (too far north; Carvajal et al., 2017) ruptures as sources for the tsunami and concluded that the sand bed was likely deposited by a tsunami associated with the 1835 AD rupture. Bracketing radiocarbon ages for the third oldest sand bed (sand bed 4 in this study) at Tirúa (1640–1800 AD) suggest that the 1835 AD tsunami is not preserved at the site. Based on regional historical accounts and the bracketing radiocarbon ages, Ely et al. (2014) instead attributed the third oldest sand bed at Tirúa to a tsunami associated with the 1751 AD rupture. At Quidico, the fourth oldest sand bed (sand bed 4 in this study; modeled age range of 1690–1910 AD) was also attributed to the 1751 AD rupture and tsunami. The age of the fourth oldest sand bed (sand bed 5 in this study) at Tirúa (1500–1630 AD) overlaps with two historical tsunamis in 1570 AD and 1575 (Ely et al., 2014). Ely et al. (2014) interpreted this sand bed as more likely to be associated with the 1575 rupture, which historical records indicate was larger than the 1570 AD tsunami. The Quidico record does not contain the 1575 AD tsunami. Instead, the fifth oldest sand bed (sand bed 7 in this study) at Quidico (modeled age range of 1445–1490 AD) precedes the historical tsunami record. An OSL dating study of the Tirúa sand sequence yielded a similar chronology to that reported in Ely et al. (2014) for the youngest three sand beds (sands 1, 2, and 4 in this study), however the older sand beds yielded significantly older ages (Nentwig et al., 2015).

In a comparison of the Quidico and Tirúa tsunami chronologies, Hong et al. (2017) noted that the preservation of the 1835 tsunami and the absence of the 1575 tsunami differentiate the Quidico record from the Tirúa record. Hong et al. (2017) inferred that the coastal morphology of the two study sites influences the completeness of the stratigraphic records of tsunamis preserved at each site. The Tirúa River drains into the Pacific Ocean at a northwestward facing embayment, leaving it vulnerable to tsunamis generated from both northern ruptures (e.g., 2010 and 1751) and southern ruptures (e.g., 1960 and 1575). In contrast, the mouth of the Quidico River is protected by bedrock to the south and west, creating a northward-facing embayment that selectively preserves tsunamis propagating from the north (e.g., 2010, 1835, 1751) (Fig. 2a).

2.4. Reconstructing land-level change at the Tirúa and Quidico estuaries

Despite the detailed stratigraphic and chronological framework for tsunami inundation at Tirúa and Quidico provided by Ely et al. (2014) and Hong et al. (2017), questions about the nature of coseismic and interseismic land-level change at Tirúa and Quidico remain, which impact the correlation of tsunami events between sites and the interpretation of rupture extents during historical earthquakes. Our new diatom-based coseismic and interseismic land-level change reconstructions test the previously inferred correlations of the tsunami sand beds between Tirúa and Quidico, expand the earthquake records at the sites, and provide further insight into the slip distribution of past ruptures.

To reconstruct the paleoenvironmental history of the Tirúa and Quidico estuaries and identify past coseismic and interseismic RSL changes and tsunami inundation, we collected monoliths (6 × 5 × 50 cm columns of sediment) from two representative stratigraphic sections at Tirúa (sections T16 and T2, separated by ~130 m) and Quidico (sections Q9 and Q13, separated by ~150 m) for high-resolution grain size, loss on ignition (LOI), and diatom analyses (Figs. 2, 3; Table 1 Appendix 1). All sections were photographed and their lithology, color (Munsell soil color charts, 1975), and stratigraphy described in the field. Tirúa sections T16 and T2 and Quidico section Q9 are riverbank exposures, while Quidico section Q13 was collected from an abandoned meander. We

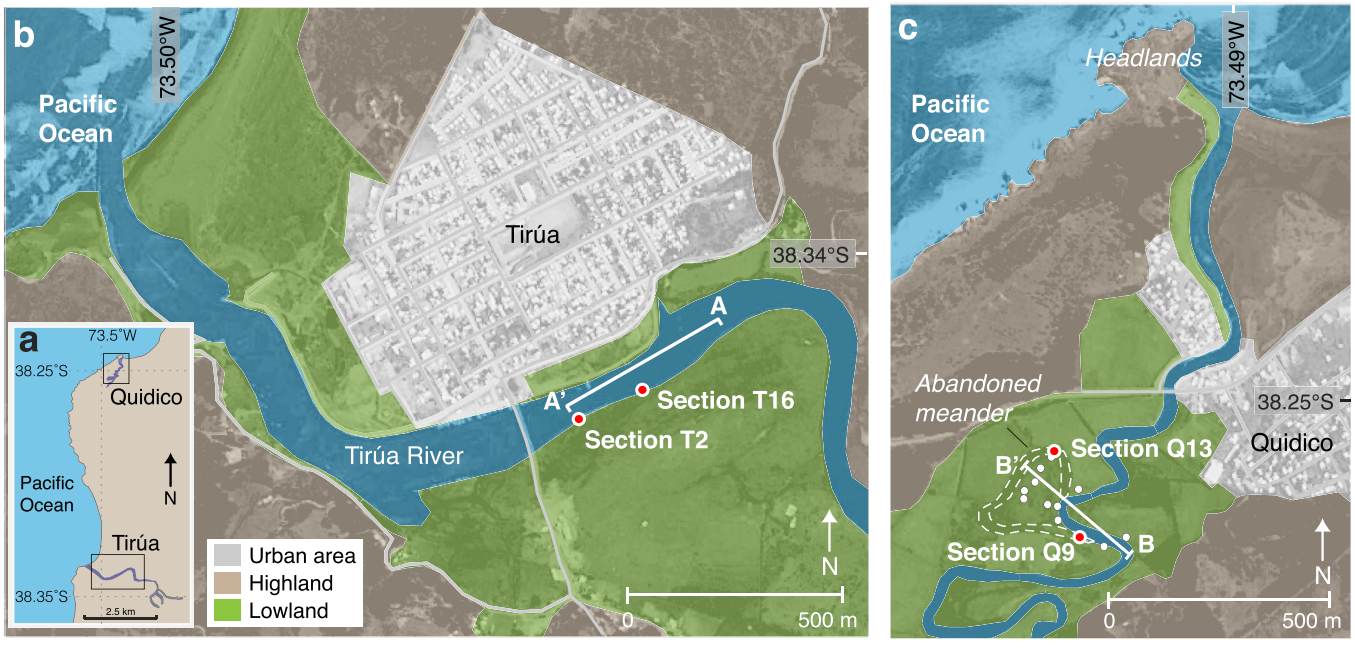

Fig. 2. a) The Tirúa and Quidico rivers are located about 160 km and 170 km south of Concepción, respectively. b) Satellite Google Earth Pro, 2014 DigitalGlobe imagery of the Tirúa River lowland with color overlay to highlight geomorphic features. Riverbank transect A-A′ is bracketed in white. Red dots show location of sections T16 and T2. c) Satellite Google Earth Pro, 2014 DigitalGlobe imagery of the Quidico River lowland with color overlay to highlight geomorphic features. Red dots show location of sections Q9 and Q13. Described cores and sections (white dots) were projected onto elevation transect B-B′, bracketed in white. (For interpretation of the references to colour in this figure legend, the reader is referred to the web version of this article.)

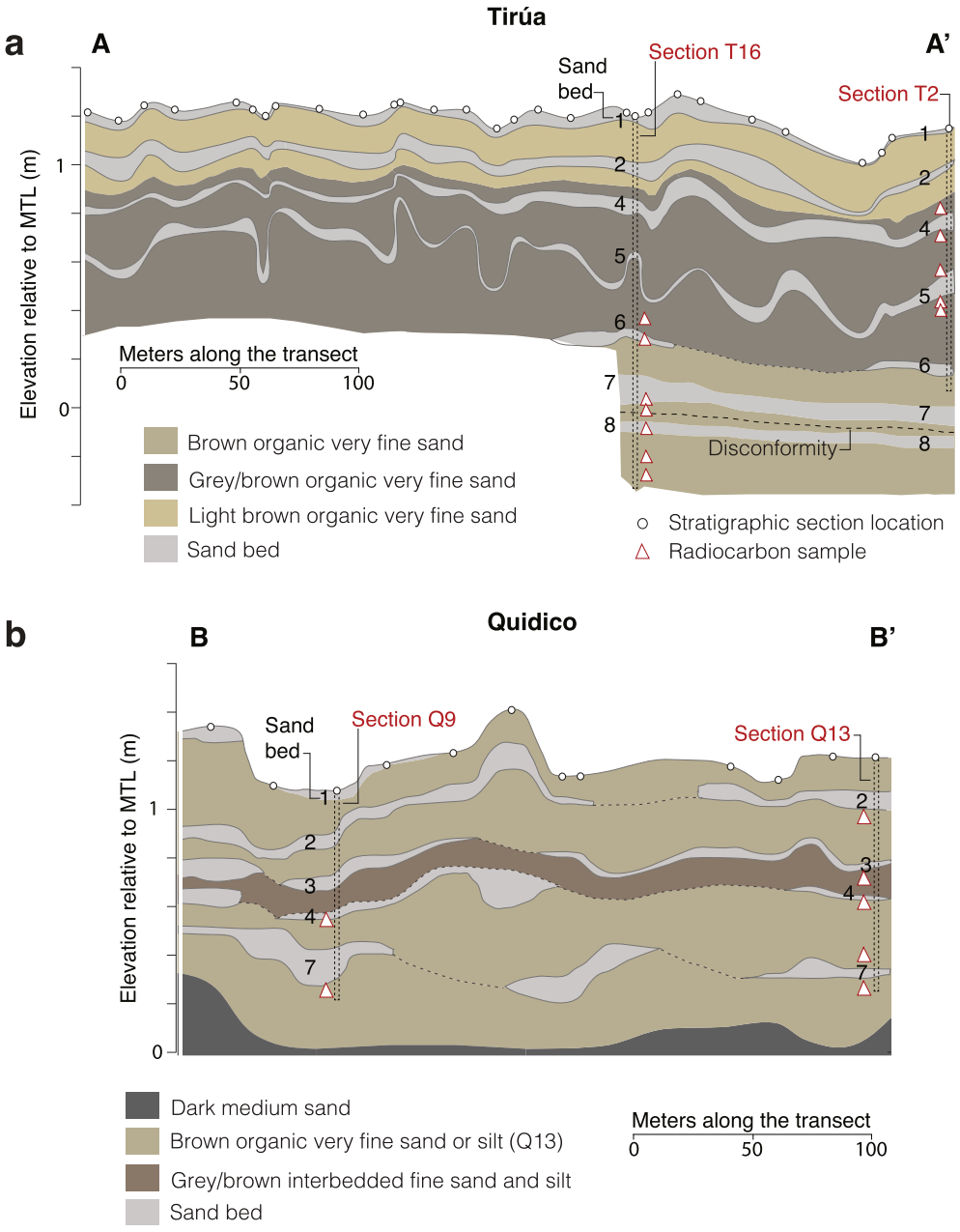

Fig. 3. Correlated stratigraphic units in transect A-A′ at Tirúa (a) and B-B′ at Quidico (b) (see Fig. 2b and c for transect locations). Circles show stratigraphic section locations and triangles show radiocarbon sampling locations. Elevations are relative to mean tidal level (MTL). Sections chosen for detailed analysis (T16, T2, Q9, and Q13) are highlighted in red. (For interpretation of the references to colour in this figure legend, the reader is referred to the web version of this article.)

analyzed two stratigraphic sections to replicate our results at each site (e.g., Shennan et al., 2016). The elevations of described and sampled stratigraphic sections were tied into benchmarks and tidal datums established by Ely et al. (2014) and Hong et al. (2017), and reported as elevation (in meters) relative to mean tide level (MTL).

We defined fossil diatom assemblage zones below and above sand beds using a stratigraphically constrained incremental sum-of-squares (CONISS) cluster analysis. We also applied detrended correspondence analysis (DCA) to examine the pattern of diatom assemblage variation between samples (e.g., Horton and Edwards, 2006; Cochran et al., 2007). Samples with similar species compositions are grouped together in the DCA bi-plot and samples with statistically different species compositions plot apart (e.g., Birks, 1986, 1992).

2.5. Dating and correlation of inferred coseismic land-level change

To develop a chronology for the prehistoric sand beds preserved at Tirúa, we collected plant macrofossils from organic-rich sediments for radiocarbon dating that were in growth position (rhizomes) or so delicate (e.g., seeds, leaf parts) that they would probably have decayed or been broken by transport soon after death, thus reducing the likelihood of dating material much older than sample burial (e.g., Kemp et al., 2013). The macrofossils yielded either limiting maximum ages (detrital or growth position below each contact) or limiting minimum ages (in growth position above each contact; Figs. 5 and 6).

We estimated the age range for deposition of sand beds 6, 7, and 8 using a bespoke Bayesian age model (Appendix 1) with all but one

Table 1
Ecology of diagnostic diatom species in sections T16, T2, Q9, and Q13.

Species (>5% abundance)	Ecology[a]	Ecology[b]	Life form[c]
Achnanthes brevipes	B & M	M & B	Epiphytic
Actinocyclus normanii	B	B	Planktonic
Actinoptychus senarius	M	M	Planktonic
Amphora coffeaeformis	B	–	Epipelic
Amphora ovalis	FW	FW	Epipelic
Bacillaria sp.	M	–	Epipelic
Caloneis bacillum	FW	–	Epipelic
Cavinula lapidosa	FW	–	Epipelic
Cocconeis neodiminuta	B	–	Epipsammic
Cocconeis placentula	–	FW & B	Epiphytic
Cosmioneis pusilla	FW & B	FW & B	Aerophilic & Epiphytic
Cymbella descripta	FW	FW	Epipelic
Delphineis kippae	M	–	Tychoplanktonic
Delphineis surirella	M & B	M	Tychoplanktonic
Denticula subtilis	B	–	Epipelic
Diploneis bombus	M & B	M & B	Epipelic
Diploneis psuedovalis	FW & B	–	Epipelic
Diploneis smithii	B & M	B & M	Epipelic
Eunotia intermedia	FW	–	Epipelic
Eunotia praerupta	FW	–	Epipelic
Fallacia forcipata	B	–	Epipelic
Fallacia pygmaea	B	–	Epipelic
Fragilaria subsalina	B	–	Epipelic
Gomphonema parvulum	FW & B	FW	Aerophilic & Epiphytic
Gyrosigma nodiferum	B & FW	B	Epipelic
Hantzschia amphioxys	FW & B	FW & B	Aerophilic
Hyalodiscus scoticus	M	M & B	Epiphytic
Karayevia oblongella	FW	–	Epipelic
Luticola mutica	FW & B	FW & B	Aerophilic
Navicula cari	FW & B	–	Epipelic
Navicula cincta	B	M & B	Epipelic
Navicula peregrina	B	M & B	Epipelic
Navicula phyllepta	B	M & B	Epipelic
Navicula rhynchocephala	FW & B	B	Epipelic
Navicula tripunctata	FW & B	–	Epipelic
Neidium alpinum	FW	–	Epipelic
Nitzschia amphibia	FW & B	FW	Aerophilic & Epiphytic
Nitzschia frustulum	FW & B	–	Aerophilic & Epiphytic
Odontenlla aurita	M	–	Tychoplanktonic
Opephora pacifica	M	M & B	Epipsammic
Paralia sulcata	M & B	M	Planktonic
Pinnularia brandelii	FW	–	Epipelic
Pinnularia brevicostata	FW & B	–	Epipelic
Pinnularia ignobilis	FW	–	Epipelic
Pinnularia intermedia	FW	–	Epipelic
Pinnularia lagerstedtii	FW	–	Epipelic
Pinnularia nodosa	FW	–	Epipelic
Planothidium delicatulum	B	B & M	Epipsammic
Psuedostaurosira brevistriata	FW	FW & B	Tychoplanktonic
Rhaphoneis amphiceros	M	M	Tychoplanktonic
Rhopalodia acuminata	B	–	Epiphytic
Rhopalodia brebissonii	B	–	Epiphytic
Rhopalodia gibberula	FW	–	Epiphytic
Staurosira construens	FW & B	FW & B	Tychoplanktonic
Thalasiasora angulata	–	M	Planktonic
Thalasiasora pacifica	–	M	Planktonic
Thalasiasora tenera	–	M	Planktonic
Tryblionella levidensis	B	–	Epipelic

[a] From Chilean (e.g., Rivera, 2000; Rebolledo et al., 2005, 2011) and global (e.g., Krammer and Lange-Bertalot, 1986, 1988, 1991a,b; Denys, 1991; Vos and de Wolf, 1993; Hartley et al., 1986; Lange-Bertalot, 2000) catalogs.
[b,c] From Vos and de Wolf (1993). Planktonic = diatoms that float freely in the water column and do not live attached to any substrate; Tychoplanktonic = diatoms that live in the benthos, but are commonly found in the plankton; Epipelic = diatoms that live on or just below the surface of wet muddy sediments; Epiphytic = diatoms that are attached to larger plants or other surfaces; Aerophilic = diatoms that are able to survive subaerial, temporarily dry conditions.

of the calibrated radiocarbon ages for the sand beds at the two sites. The one outlier sand bed age (Sample 9; Table 2, Fig. 4) was probably reworked from below an unconformity between sand beds 8 and 7. The Bayesian age model is adapted from the phase modeling approach of Buck et al. (1996) and Bronk Ramsey (2008). The model calibrates sand bed radiocarbon ages simultaneously, using the Southern Hemisphere Radiocarbon Calibration Curve of Hogg et al. (2013). The age of each sand bed is modeled between the calibrated probability distributions of the maximum limiting and minimum limiting ages for each sand bed. We fit the model to each of the sand bed radiocarbon ages to create a posterior probability distribution for the age model of the sand bed given the surrounding ages (Fig. 4). We then report these posterior probability distributions using 95% probability intervals, but the full access to the posterior distribution further allows us to calculate differences between related sand beds and other recurrence relations.

We correlated historical sand beds between Tirúa and Quidico following the tsunami chronologies of Ely et al. (2014) and Hong et al. (2017; Table 2). We correlated prehistoric sand beds between sites using our age models for sand bed deposition, and by matching the direction of land-level change coincident with sand beds indicated by our diatom analyses.

3. Results

3.1. Stratigraphic overview

Stratigraphy at Tirúa consists of seven gray (10 YR 5/1) 2 to 15-cm-thick fine sand beds (sand beds 1, 2, 4, 5, 6, 7, and 8) interbedded within organic (containing humified organic matter) very fine sand units varying in color from brown (10 YR 4/3) to gray brown (10 YR 5/2) to light brown (10 YR 6/3) (Fig. 3a). The most complete stratigraphic section (section T16) preserves sediments as old as ~1800 years. However, radiocarbon ages reveal a probable disconformity between sand beds 8 and 7. A prominent bench along the riverbank containing leaves, stems, and logs protrudes immediately below sand bed 8. Radiocarbon ages from the top of this bench and those from sediments immediately underlying sand bed 7 are separated by ~1000 years but by only 8 cm of sediment (Fig. 5a). The disconformity is also reflected in the diatom composition of sediments within the bench and immediately underlying sand bed 7; tidal flat and marine planktonic and littoral diatoms dominate sediments within the bench while sediments above the bench contain many more freshwater and brackish epipelic and epiphytic diatoms (Fig. 7; Table 1). Radiocarbon ages from sediments immediately below sand bed 7 to the top of the section suggest continuous sedimentation (Table 2; Fig. 4).

At Quidico, the stratigraphy consists of five gray (10 YR 5/1) 3 to 15-cm-thick fine sand beds (sand beds 1, 2, 3, 4, and 7) interbedded within organic very fine sand or interbedded sand and silt (Pit Q9), and silt (Pit Q13) units ranging in color from brown (10 YR 4/3) to gray brown (10 YR 5/2) (Fig. 3b). Radiocarbon ages from both stratigraphic sections described at Quidico suggest ~600 years of continuous sedimentation.

The eight sand beds preserved at the Tirúa and Quidico sites were distinct from the surrounding organic units due to their sharp (<1–3 mm) upper and lower contacts, lack of organic matter, greater mean grain size, uniform thickness, anomalous marine and brackish diatoms, and >300 m lateral extent (Tables 3 and 4). We have labeled the sand beds from youngest (1) to oldest (8) (Figs. 3, 5 and 6). Sand beds preserved and correlated between sites were assigned the same number (e.g., sand bed 1 at Tirúa and sand bed 1 at Quidico were both deposited by the 2010 tsunami).

Downcore diatom assemblages fluctuate back and forth between marine and/or brackish dominated assemblages and brackish and/or freshwater assemblages coincident with the widespread, anomalous sand beds preserved at Tirúa and Quidico. These sudden changes in diatom composition are consistent with repeated abrupt RSL changes affecting the marshes fringing the

Table 2
Radiocarbon data for ages from Tirúa and Quidico.

Sand bed	Calibrated age (yr AD - 2σ) [a]	Maximum or minimum limiting age[b]	Description of dated material	Section[c]	Sample no. [d]	Elevation MTL (m)	Lab reported age (^{14}C yr BP)	Radiocarbon Laboratory number[e]	Used in age model?
Tirúa									
4	**1640-1800**	minimum	Charcoal fragment 1cm above sand bed 4	2	1*	0.77	250 ± 25	OS-94872	Historical*
4	**1460-1640**	maximum	Charcoal fragment below sand bed 4	2	2*	0.62	360 ± 40	Beta-276184	Historical*
5	**1440-1630**	minimum	Wood fragment above Sand bed 5	2	3*	0.5	430 ± 40	Beta-261094	Historical*
5	**1410-1450**	maximum	Rhizome sheath immediately below sand bed 5	2	4*	0.41	530± 25	OS-94871	Historical*
5	**1500-1630**	maximum	*Calystegia seed 5 cm below Sand bed 5Calystegia seed 5 cm below Sand bed 5*	2	5*	0.38	365 ± 15	PRI-Tirúa 012413-2	Historical*
6	**1450-1620**	minimum	8 seed casings above sand bed 6	16	6	0.34	420 ± 20	OS-111755	Yes
6	**1510-1950**	maximum	11 (possible) fruit pods below sand bed 6	16	7	0.28	245 ± 55	OS-112553	
7	**1440-1490**	maximum	*In situ rhizome below sand bed 7In situ rhizome below sand bed 7*	2	8	0.05	460±20	OS-102372	Yes
7	**420-530**	maximum	10 Schoenoplectus sp. seeds below sand bed 710 Schoenoplectus sp. seeds below sand bed 7	16	9	0.05	1630 ± 20	OS-111756	No
8	**420-530**	minimum	9 Schoenoplectus sp. seeds above sand bed 89 Schoenoplectus sp. seeds above sand bed 8	16	10	0.02	1630 ± 20	OS-111757	Yes
8	**240-360**	maximum	4 Schoenoplectus sp. seeds and 2 round seeds below sand bed 84 Schoenoplectus sp. seeds and 2 round seeds below sand bed 8	16	11	-0.05	1790 ± 20	OS-111758	Yes
Base of section	**250-380**	maximum	4 leaf fragments at base of section	16	12	-0.19	1760 ± 25	OS-111759	Yes
Base of section	**130-310**	maximum	9 leaf fragments at base of section	16	13	-0.25	1850 ± 20	OS-111760	Yes
Quidico									
2	**modern**	maximum	5 Schoenoplectus sp. seeds below sand bed 2	13	14**	0.94	65 ± 30	OS-103406	Historical**
3	**modern**	maximum	16 Schoenoplectus sp. seeds below sand bed 3	13	15**	0.7	105 ± 25	OS-103407	Historical**
4	**1670-present**	maximum	5 Schoenoplectus sp. seeds below sand bed 4	13	16**	0.57	185 ± 25	OS-103408	Historical**
7	**1430-1610**	minimum	12 Schoenoplectus sp. seeds above sand bed 7	13	17**	0.48	460 ± 30	OS-106356	Yes
7	**1320-1450**	maximum	11Potamogeten sp. seeds below sand bed 7	13	18**	0.34	570 ± 45	OS-103409	Yes
4	**1650-1800**	maximum	6 Schoenoplectus sp. seeds below sand bed 4	9	19**	0.57	245 ± 15	OS-115319	Historical**
7	**1430-1450**	maximum	12.5 Schoenoplectus sp. seeds below sand bed 7	9	20**	0.34	495 ± 15	OS-115318	Yes
Base of section	**1450-1610**	minimum	5 Schoenoplectus sp. seeds above basal sand	13	21**	0.26	425 ± 15	OS-106268	Yes
Base of section	**1430-1480**	minimum	9 Schoenoplectus sp. seeds above basal sand	13	22**	0.26	475 ± 20	OS-103174	Yes
Base of section	**1240-1380**	maximum	4.5 Schoenoplectus sp. seeds within basal sand	13	23**	11-25	760 ± 20	OS-103173	No

*Radiocarbon age from Ely et al. (2014).
**Radiocarbon age from Hong et al. (2017).
[a] Radiocarbon ages were calibrated using OxCal radiocarbon calibration software (Bronk Ramsey, 2008) with the SHCal13 data set of Hogg et al. (2013).
[b] Interpretation of the stratigraphic context of the dated sample relative to the time that host unit was deposited. Maximum ages are on samples containing carbon judged to be older than a sand bed. Minimum ages are on samples judged younger than a sand bed.
[c] Sections with corresponding radiocarbon age locations can be found on Fig. 3a and b.
[d] Sample ID's and corresponding sampling locations can be found on Fig. 4a and b and Fig. 5a and b.
[e] Samples with the prefix OS- were analyzed by the NOSAMS facility at Woods Hole Oceanographic Institution, and those with Beta-were analyzed at Beta Analytic.

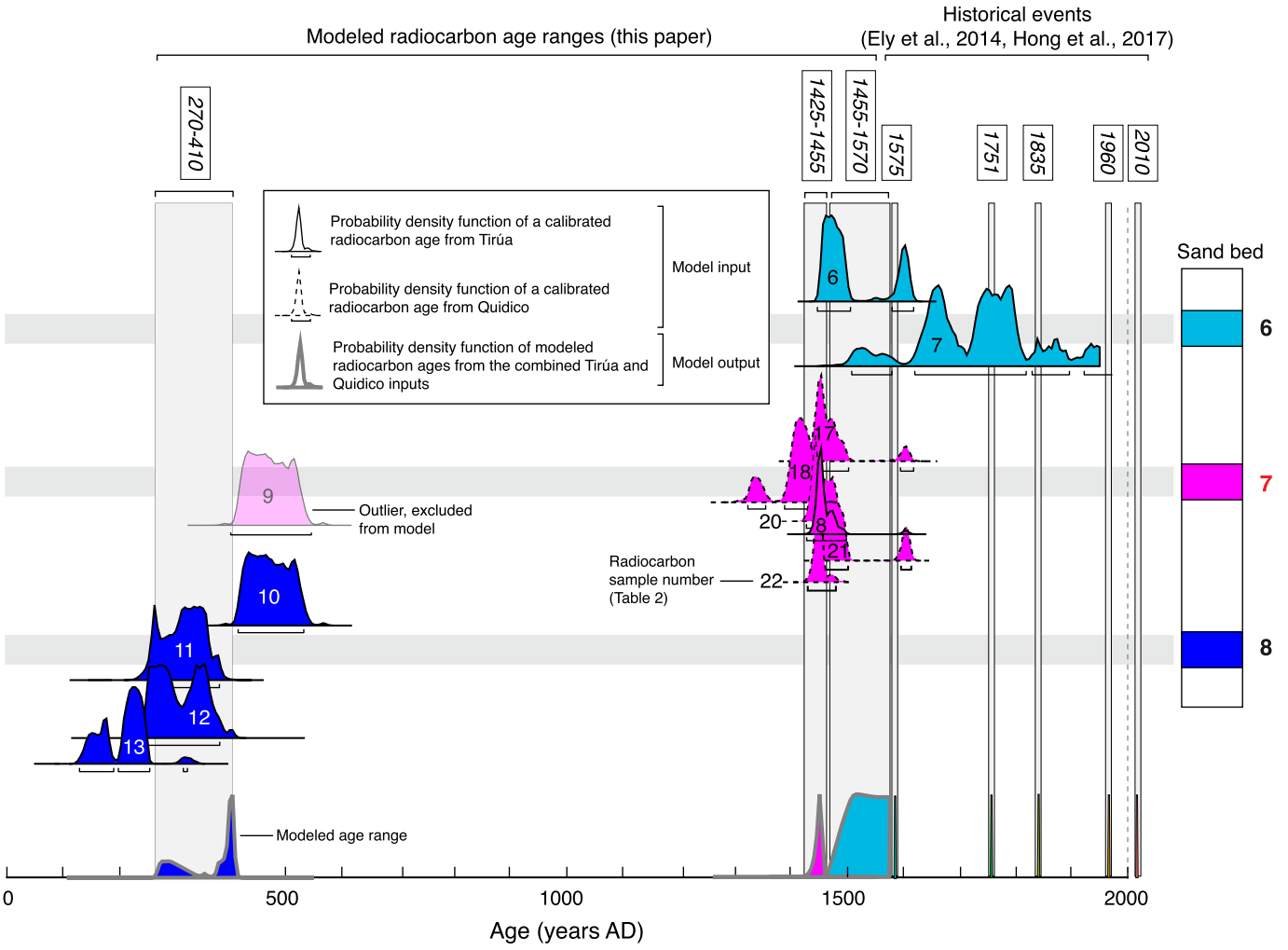

Fig. 4. Bayesian chronology age models for the times that sand beds 6, 7, and 8 were deposited at Tirúa and Quidico. Calibrated probability distribution functions (pdfs) for each limiting radiocarbon age are shown for each bed (vertical axis not to scale). Age models developed using R software (R Core Team, 2016; available on GitHub at https://github.com/andrewcparnell/sand_beds). We approximate the model fitting stage by breaking up the model and fitting it to each individual sand bed. Each sand bed posterior distribution can be plotted as a probability distribution histogram, or summarize into mean, standard deviation, and credibility interval. 95% credibility intervals are reported as standard.

sites during past great earthquakes. Below, we describe the sedimentary, diatom, and chronological results from each sand bed and the under-and-overlying material.

3.1.1. Sand bed 8 (Tirúa)

A brown, poorly sorted interbedded organic and clean very fine sand underlies sand bed 8 at Tirúa (Fig. 5a). Marine planktonic, epipsammic, and epiphytic diatoms dominate the assemblage in both the organic sand and clean sand layers (Fig. 7; Table 3). Minor abundances of freshwater epipelic and epiphytic diatoms are also present. Leaf fragments collected from the base of section T16 yield ages of 130–310 AD and 250–380 AD for the oldest sediments described in section T16 (Fig. 5a; Table 2).

A sharp contact separates a clean, gray, fine sand (sand bed 8) from the underlying organic sand. Sand bed 8 displays an increase in mean grain size and a decreased fine fraction (D10) and organic content (LOI; Fig. 5a). The sand bed contains a mixed diatom assemblage composed of marine, brackish, and freshwater taxa (Fig. 7).

A brown, poorly sorted organic very fine sand overlies sand bed 8. The organic sand contains an increase in freshwater epipelic and epiphytic, and brackish epipelic and epipsammic taxa compared to the marine dominated assemblage underlying the sand bed. The decreased marine influence above sand bed 8 is reflected by an increase in LOI and the ratio of freshwater to marine and brackish diatoms, and a decrease in the percentage of marine and brackish planktonic diatoms (Figs. 5 and 9; Table 3). Constrained cluster and DCA analyses reflect the shift in diatom species composition from marine dominated samples below sand bed 8 to freshwater and brackish dominated samples above the sand bed (Figs. 7 and 8a).

Schoenoplectus sp. seeds collected from the organic sand immediately underlying and overlying sand bed 8 in T16 yield a maximum limiting age of 240–360 AD and a minimum limiting age of 420–530 AD for sand deposition (Fig. 5a; Table 2).

3.1.2. Sand bed 7 (Tirúa and Quidico)

A brown, poorly sorted organic very fine sand (sections T16 and Q9) or silt (section Q13) underlies sand bed 7 (Figs. 5a and 6). Freshwater epipelic and fresh-brackish epiphytic taxa and minor abundances of brackish epipelic taxa make up the diatom assemblage in the organic sand/silt at both Tirúa and Quidico (Figs. 7, 10, Fig. A4; Tables 3 and 4).

A sharp contact separates a clean, gray, well-sorted fine sand (sand bed 7) from the underlying organic sand/silt. Sand bed 7

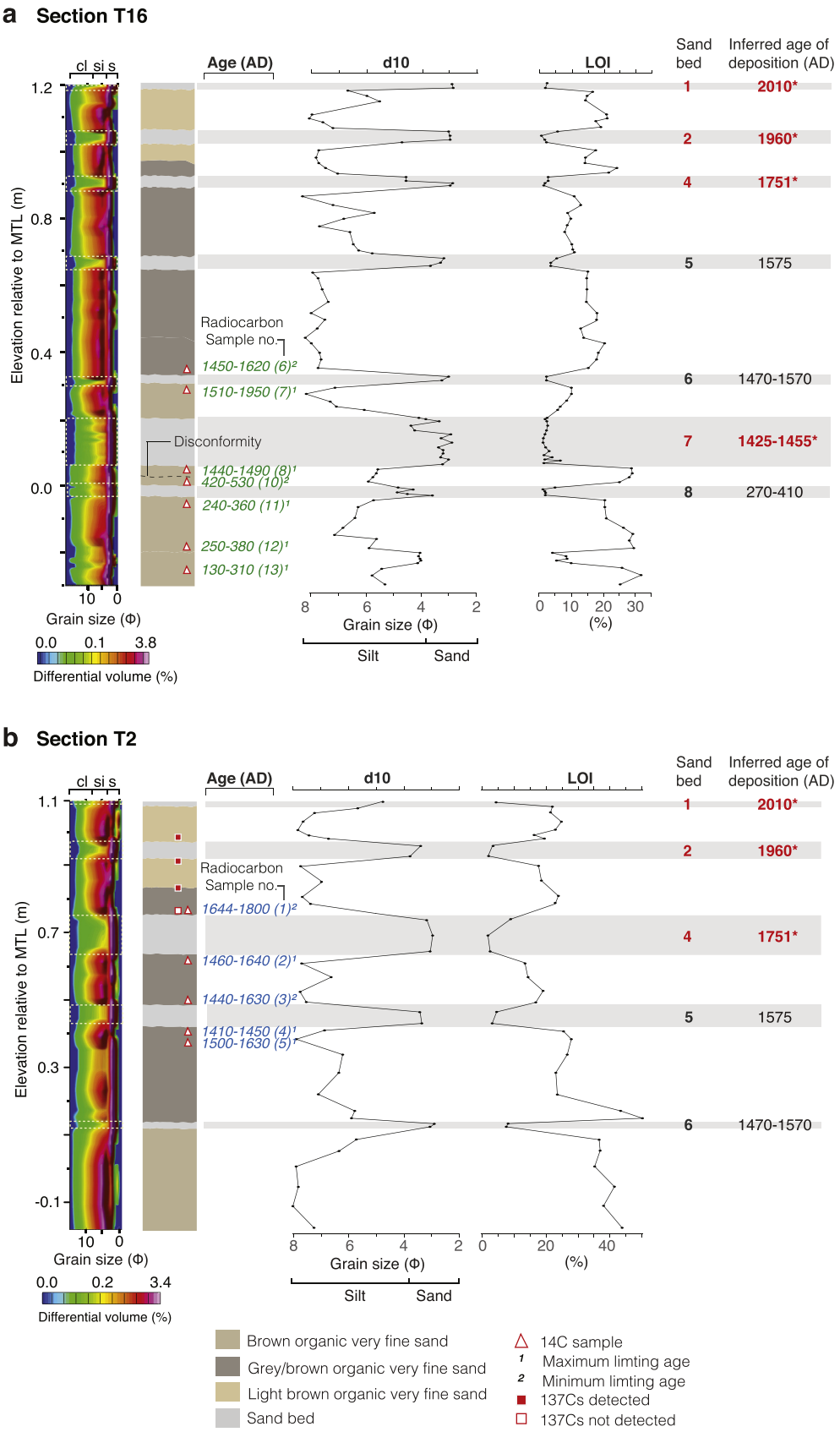

Fig. 5. a,b) High-resolution grain-size distribution color surface plots (Φ) showing the differential volume of sediments (the percentage of total volume that each size class occupies), D10 values (diameter at which 10% of a sample's mass is comprised of smaller grains), and LOI (weight % of organic material) for stratigraphic columns of sections T16 and T2. Elevations are relative to mean tide level (MTL). Radiocarbon sampling locations and calibrated radiocarbon ages are plotted on columns. Radiocarbon age determinations from this study are in green and ages from Ely et al. (2014) are in blue. Radiocarbon sample numbers correspond to sample numbers in Table 2. ^{137}Cs analysis is from Ely et al. (2014). Inferred timing of coseismic land-level change and sand bed deposition, constrained by our age model, is shown for each event. (For interpretation of the references to colour in this figure legend, the reader is referred to the web version of this article.)

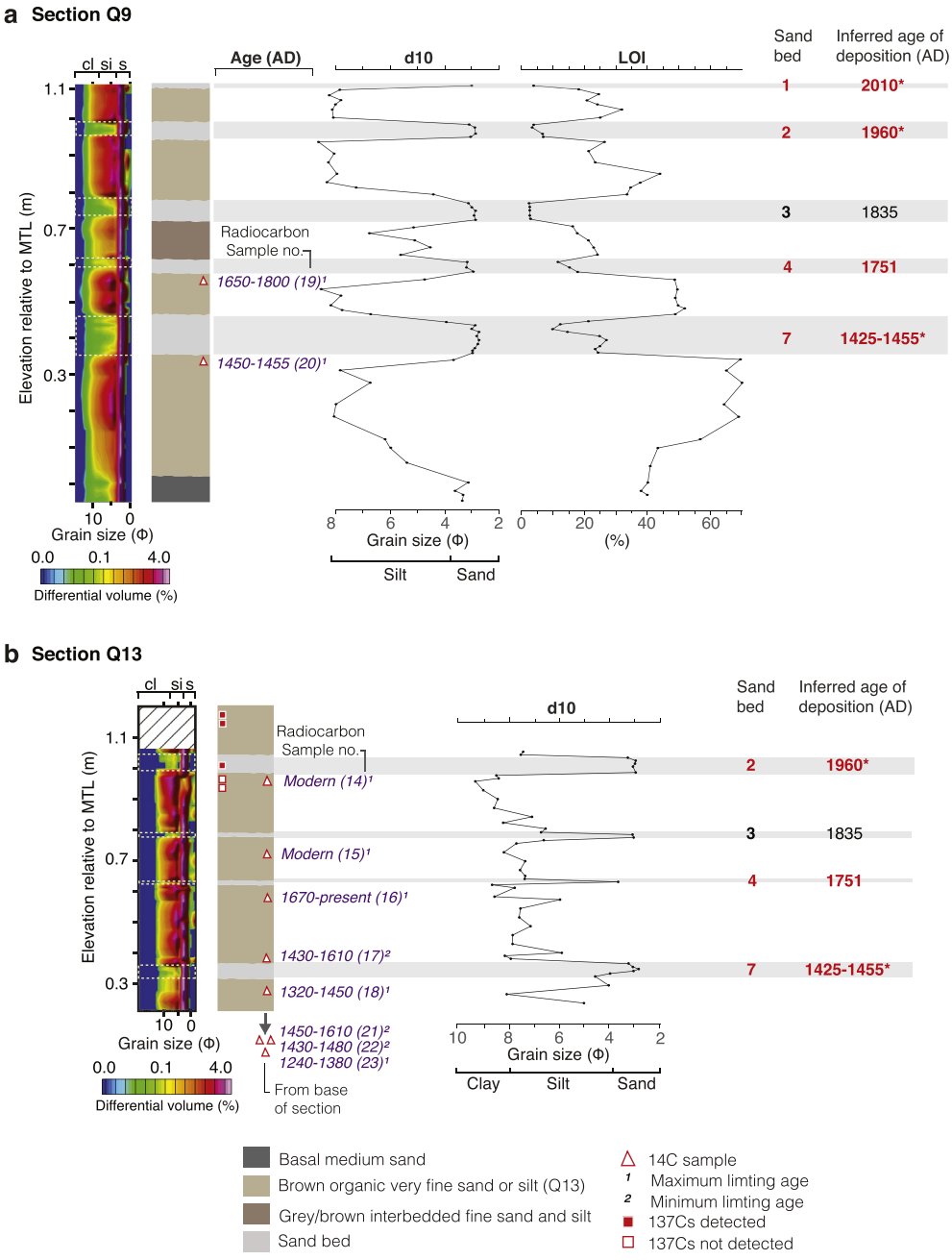

Fig. 6. a,b) High-resolution grain-size distribution color surface plots (Φ) showing the differential volume of sediments (the percentage of total volume that each size class occupies), D10 values (diameter at which 10% of a sample's mass is comprised of smaller grains), and LOI (weight % of organic material) for stratigraphic columns of sections Q9 and Q13. Elevations are relative to mean tide level (MTL). Radiocarbon sampling locations and calibrated radiocarbon ages are plotted on columns. Radiocarbon age determinations from Hong et al. (2017) are in purple. Radiocarbon sample numbers correspond to sample numbers in Table 2. ^{137}Cs analysis is from Hong et al. (2017). Inferred timing of coseismic land-level change and sand bed deposition, constrained by our age model, is shown for each event. (For interpretation of the references to colour in this figure legend, the reader is referred to the web version of this article.)

displays an increase in mean grain size and a decreased fine fraction (D10) and organic content (LOI; Figs. 5a and 6). The sand bed contains a mixed diatom assemblage composed of marine, brackish, and freshwater taxa, with a distinctive increase in marine epipsammic and planktonic taxa compared to underlying sediment at both Tirúa and Quidico (Fig. 9 and Fig. A6). At Quidico, sand bed 7 in section Q13 contains small percentages of anomalous marine tychoplanktonic diatoms not found in the underlying or overlying sediment (Fig. A4).

A brown, poorly sorted organic very fine sand (sections T16 and Q9) or silt (section Q13) overlies sand bed 7. The organic sand/silt contains an increase in marine planktonic and brackish epipelic taxa compared to the freshwater and brackish dominated assemblage underlying sand bed 7. The increased marine influence above sand bed 7 is reflected by a fall in LOI and the ratio of freshwater to marine and brackish diatoms, and an increase in the percentage marine and brackish planktonic diatoms (Figs. 5a, 6 and 9, Fig. A4; Tables 3 and 4). Constrained cluster and DCA analyses reflect the shift in diatom species composition from freshwater dominated samples below sand bed 7 to brackish and marine dominated

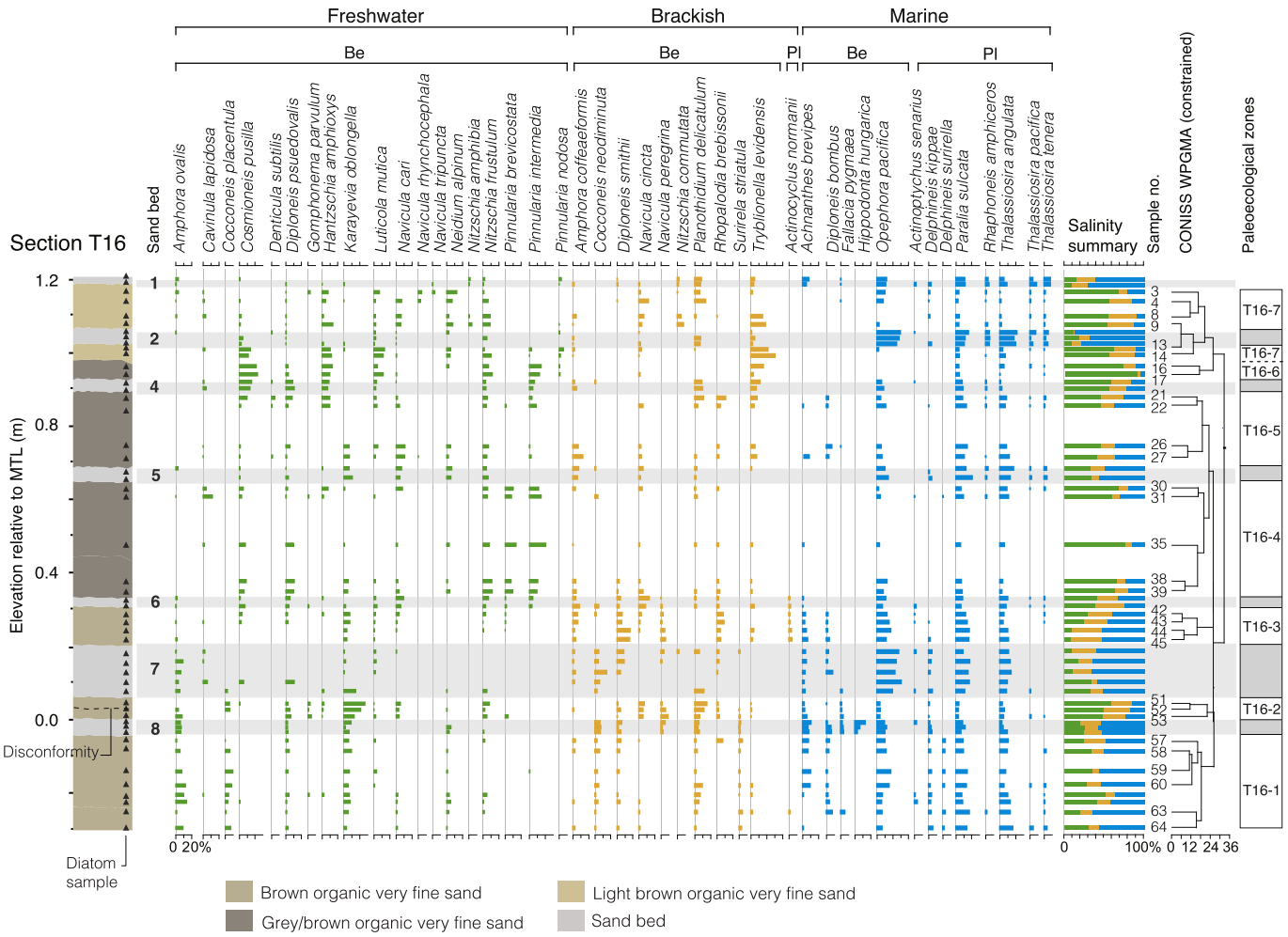

Fig. 7. Relative abundance of diatoms (showing only those species >5% abundance) for section T16. Relative abundance is expressed as a percent of the total count. Triangle symbols on stratigraphic column show locations of numbered samples (sample numbers shown to the right of the salinity summary). The results of the stratigraphically constrained incremental sum-of-squares (CONISS) cluster analysis are shown beside our interpretation of paleoecological zones. Be: benthic; Pl: planktonic.

samples above the sand bed (Fig. 8 and Fig. A5).

An *in situ* rhizome collected from the organic sand immediately underlying sand bed 7 at Tirúa provides a maximum age of deposition of 1440–1490. *Schoenoplectus* sp. and *Potamogeten* sp. seeds underlying and *Schoenoplectus* sp. seeds overlying sand bed 7 at Quidico yield maximum limiting ages of 1430–1450 AD, and 1320–1450 and a minimum limiting age of 1430–1610, respectively (Figs. 5a and 6; Table 2).

3.1.3. Sand bed 6 (Tirúa)

A brown, poorly sorted organic very fine sand underlies sand bed 6 (Fig. 5). Marine planktonic and epipsammic, and brackish epipelic taxa dominate the diatom assemblage in the organic sand at Tirúa (Fig. 7 and Fig. A1; Table 3).

A sharp contact separates a clean, light-gray, well-sorted fine sand (sand bed 6) from the underlying organic sand. Sand bed 6 displays an increase in mean grain size and a decreased fine fraction (D10) and organic content (LOI; Fig. 5). The sand bed contains a mixed diatom assemblage composed of marine, brackish, and freshwater taxa (Fig. 7 and Fig. A1).

A gray brown, poorly sorted organic very fine sand overlies sand bed 6. The organic sand contains an increase in freshwater epipelic and fresh-brackish epiphytic taxa compared to the marine and brackish dominated assemblage underlying sand bed 6. The decreased marine influence above sand bed 6 is reflected by an increase in LOI and the ratio of freshwater to marine and brackish diatoms, and a decrease in the percentage of marine and brackish planktonic diatoms (Figs. 5, 9, Fig. A3; Table 3). Constrained cluster and DCA analyses reflect the shift in diatom species composition from marine and brackish dominated samples below sand bed 6 to freshwater dominated samples above the sand bed (Figs. 7, 8a, Fig. A1 and A2).

Seed casings collected from the organic sand immediately above sand bed 6 yield a minimum limiting age of 1450–1620 AD for sand deposition (Fig. 5; Table 2).

3.1.4. Sand bed 5 (Tirúa)

A gray-brown, poorly sorted organic very fine sand underlies sand bed 5 (Fig. 5). Freshwater epipelic taxa dominate the assemblage in the organic sand at Tirúa (Fig. 7 and Fig. A1; Table 3).

A sharp contact separates a clean, gray, well-sorted fine sand (sand bed 5) from the underlying organic sand. Sand bed 5 displays an increase in mean grain size and a decreased fine fraction (D10) and organic content (LOI; Fig. 5). The sand bed contains a mixed diatom assemblage composed of marine, brackish, and freshwater taxa, with a distinctive increase in marine epipsammic and planktonic taxa compared to underlying sediment at Tirúa (Fig. 9 and Fig. A3).

Table 3
Results summary: Tirúa.

Tirúa sections*	Unit or sand bed	Mean (Φ)[a]	D10 (Φ)[b]	LOI (%)[c]	Ratio of freshwater: marine and brackish diatoms	Diagnostic diatom results[d]	Diatom zone[e]	Inferred land-level change[f]
16/2	**Sand bed 1**	2.04/ 2.14	2.84/ 4.78	2.62/ 4.35	–	Increase in marine planktonic (*P. sulcata, T. pacifica, T. angulata, T. tenera*) and epipsammic (*O. pacifica*) diatoms.	–	
16/2	Light-brown, poorly sorted organic very fine sand	3.56/ 3.32	7.04/ 7.09	18/ 20	0.48/0.67	Similar to assemblage below Sand bed 2	T16-7/ T2-5	No change
16/2	**Sand bed 2**	2.31/ 2.23	3.41/ 3.54	3.13/ 2.54	–	Increase in marine planktonic (*D. kippae, P. sulcata, T. angulata, T. pacifica*) and epipsammic (*O. pacifica*) diatoms.	–	
16/2	Light-brown or grey-brown, poorly sorted organic very fine sand	3.9/ 3.82	7.58/ 7.12	13/ 20	0.45/0.80	Slight decrease in freshwater and increase in brackish epipelic (*N. cincta, R. brebissonii, T. levidensis*) diatoms.	T16-7/ T2-5	
16 and 2	Grey-brown, poorly sorted organic very fine sand	3.8/ 3.71	7.58/ 6.94	20/ 40	9.0/2.5	Increase in freshwater diatoms: *C. pusilla, D. psuedovalis, H. amphioxys, L. mutica, P. intermedia, N. Frustulum.*	T16-6/ T2-4	Uplift
16/2	**Sand bed 4**	2.33/ 2.20	3.76/ 2.96	2.58/ 4.35	–	Mixed assemblage: *O. pacifica, C. pusilla, D. psuedovalis, Hantzschia amphioxys, P. sulcata, P. delicatulum, T. angulata, T. levidensis.*	–	
16/2	Grey-brown, poorly sorted organic very fine sand	3.49/ 3.64	6.8/ 7.35	10/ 22	0.83/0.35 0.65/0.34	Similar to assemblage above Sand bed 5 Increase in marine epipsammic (*O. pacifica*), epiphytic (*A. brevipes*), and brackish epipelic (*A. coffeaeformis, D. smithii, F. subsalina, N. cincta, T. levidensis*) diatoms.	T16-5/ T2-3	Subsidence
16/2	**Sand bed 5**	2.35/ 2.28	3.36/ 3.39	4.61/ 3.70	–	Increase in marine planktonic (*P. sulcata, T. angulata),* and epipsammic (*O. pacifica*) diatoms.	–	
16/2	Grey-brown, poorly sorted organic very fine sand	3.64/ 2.95	7.81/ 6.0	16/ 50	2.03/2.5 1.64/6.0	Similar to assemblage above Sand bed 6 Increase in freshwater diatoms: *C. pusilla, D. psuedovalis, G. Parvulum, K. oblongella, N. frustulum, P. intermedia, P. brevicostata.*	T16-4/ T2-2	Uplift
16/2	**Sand bed 6**	2.18/ 2.09	3.11/ 2.96	2.68/ 7.62	–	Mixed assemblage: *A. coffeaeformis, K. oblongella, N. cari, N. cincta, O. pacifica, P. sulcata, P. intermedia, T. angulata.*	–	
16/2	Brown, poorly sorted organic very fine sand	3.48/ 4.39	7.18/ 7.18	10/ 40	0.35/0.35 0.08/0.35	Similar to assemblage above Sand bed 7 Increase in marine planktonic (*P. sulcata, T. angulata*), epipsammic *(O. pacifica*), and brackish epipelic *(A. coffeaeformis, D. smithii, R. brebissonii*) diatoms.	T16-3/ T2-1	Subsidence
16	**Sand bed 7**	2.17	3.44	3	–	Increase in marine planktonic (*P. sulcata, T. angulata),* and epipsammic (*O. pacifica*) diatoms.	–	
16	Brown, poorly sorted organic very fine sand	3.00	5.73	25	1.31 0.91	Similar to assemblage above Sand bed 8 Increase in freshwater diatoms: *A. ovalis, D. psuedovalis, K. oblongella, G. parvulum, N. frustulum, N. cincta, N. peregrina, P. delicatulum*	T16-2	Uplift
16	**Sand bed 8**	2.40	4.43	3	–	Mixed assemblage: *O. pacifica, A. brevipes, A. ovalis, C. neodiminuta, K. oblongella, P. sulcata, T. angulata.*	–	
16	Brown, poorly sorted organic very fine sand	3.10	5.28	28	0.31	Marine diatoms (*P. sulcata, T. angulata, O. pacifica, A. brevipes*) dominate. Minor abundances of brackish and freshwater diatoms.	T16-1	

* When data for both pits are available, they are reported with a dash separating the values. Diatom results are combined for each site.
[a] Mean grain size of sand beds and underlying and overlying sediment.
[b] Dominant grain size values for the 10th (D10) percentile (diameter at which 10% of the sample volume comprises smaller particles).
[c] LOI is a proxy for the percentage of organic matter in our fossil samples.
[d] Summary of diatom results used for interpreting coseismic land-level change. Full counts included in Figs. 6, 9, Figs. A1 and A4.
[e] Diatom zones determined by using a stratigraphically constrained incremental sum-of-squares (CONISS) cluster analysis (Figs. 6, 9, Figs. A1, and A4).
[f] Inferred land-level change based on grain size, LOI, and diatom analyses.

A gray-brown, poorly sorted organic very fine sand overlies sand bed 5. The organic sand contains an increase in marine epipsammic and epiphytic taxa, and brackish epipelic taxa compared to the freshwater dominated assemblage underlying sand bed 5. The increased marine influence above sand bed 5 is reflected by a fall in LOI and the ratio of freshwater to marine and brackish diatoms, and an increase in the percentage of marine and brackish planktonic diatoms (Figs. 5, 9, Fig. A3; Table 3). Constrained cluster and DCA analyses reflect the shift in diatom species composition from freshwater dominated samples below sand bed 5 to marine and brackish dominated samples above the sand bed, although the shift is not as pronounced as other contacts in the section, reflecting a subtle change in species composition (Figs. 7, 8a, Figs. A1 and A2).

Radiocarbon dating from Ely et al. (2014) constrains the age of sand bed 5 with maximum limiting ages of 1410–1450 AD and 1500–1630 and a minimum limiting age of 1440–1630 AD (Fig. 5b, Table 2; Ely et al., 2014).

3.1.5. Sand bed 4 (Tirúa and Quidico)

A gray-brown, poorly sorted organic very fine sand (T16, T2, and Q9) or brown, poorly sorted organic silt (Q13) underlie sand bed 4 (Figs. 5 and 6). Brackish epipelic and epipsammic, and marine planktonic, planktonic, and epipsammic taxa dominate the assemblage in the organic sand/silt at both Tirúa and Quidico (Figs. 7, 10, Figs. A1 and A4; Tables 3 and 4).

A sharp contact separates a clean, gray, well-sorted fine sand (sand bed 4) from the underlying organic sand. Sand bed 4 displays an increase in mean grain size and a decreased fine fraction (D10) and organic content (LOI; Figs. 5 and 6). The sand bed contains a mixed diatom assemblage composed of marine, brackish, and freshwater taxa at Tirúa and Quidico (Figs. 7, 10, Figs. A1 and A4).

A gray-brown, poorly sorted organic very fine sand (T16 and T2), gray-brown, poorly sorted organic interbedded sand and silt (Q9), or brown poorly sorted organic silt (Q13) overlies sand bed 4. The organic sand/silt contains an increase in freshwater epipelic and fresh-brackish epiphytic diatom taxa compared to the brackish and marine dominated assemblage underlying sand bed 4 at Tirúa and Quidico. The decreased marine influence is reflected by a rise in LOI and the ratio of freshwater to marine and brackish diatoms, and a decrease in the percentage of marine and brackish planktonic

Table 4
Results summary: Quidico.

Quidico sections*	Unit or sand bed	Mean (Φ)[a]	D10 (Φ)[b]	LOI (%)[c]	Ratio of freshwater: marine and brackish diatoms	Diagnostic diatom results[d]	Diatom zone[e]	Inferred land-level change[f]
9	**Sand bed 1**	2.25	3.03	5	–	Abundant marine planktonic (*P. sulcata, T. angulata*) and epipsammic *(O. pacifica)* diatoms.	–	
9/13	Brown, poorly sorted organic very fine sand/Brown, poorly sorted organic silt	3.39/ 7.44	8.07/ 7.44	25	0.73/1.18	Similar to assemblage below Sand bed 2	Q9-6/ Q13-6	No change
9/13	**Sand bed 2**	2.26/ 3.00	3.02/ 3.01	6	–	Abundant marine planktonic (*P. sulcata, T. angulata, T. pacifica*) and epipsammic *(O. pacifica)* diatoms. Also contains anomalous marine tychoplanktonic diatoms *D. Kippae* and *D. surirella* (<2% abundance).	–	
9/13	Brown, poorly sorted organic very fine sand/Brown, poorly sorted organic silt	3.24/ 8.05	7.59/ 8.05	30	0.75/1.01	Increase in brackish epipelic (*A. coffeaeformis, C. bacillum, R. brebissonii*) and marine epipsammic (*O. pacifica*), and planktonic (*P. sulcata, T. angulata*) diatoms.	Q9-6/ Q13-6	
					1.42/1.10	Increase in freshwater epipelic (*D. psuedovalis, L. mutica, N. Frustulum, P. intermedia*) and tychoplanktonic (*P. brevistriata*).	Q9-5/ Q13-5	Uplift
9/13	**Sand bed 3**	2.29/ 3.01	2.99/ 3.01	3	–	Mixed assemblage: *D. bombus, O. pacifica, P. sulcata, T. angulata, P. delicatulum, N. cincta, T. levidensis, H. amphioxys, K. oblongella, L. mutica, N. frustulum.* Also contains anomalous marine tychoplanktonic diatom *D. surirella* (<2% abundance).	–	
9/13	Grey-brown interbedded sand and silt/Brown, poorly sorted organic silt	2.64/ 7.41	5.47/ 7.41	23	0.32/0.51	Increase in marine epipelic (*D. bombus*), epipsammic (*O. pacifica*), and planktonic (*P. sulcata, T. angulata*) diatoms.	Q9-4/ Q13-4	
					1.01/2.01	Increase in freshwater tychoplanktonic (*P. brevistriata, S. construens*) and epipelic (*D. psuedovalis, N. Frustulum, S. construens*) diatoms.	Q9-3/ Q13-3	Uplift
9/13	**Sand bed 4**	2.35/ 3.61	3.14/ 3.61	15	–	Mixed assemblage: *D. bombus, D. psuedovalis, D. smithii, N. cincta, N. peregrina, O. pacifica, P. sulcata, P. brevistriata, S. construens, R. brebissonii, T. angulata.*	–	
9/13	Brown, poorly sorted organic very fine sand/Brown, poorly sorted organic silt	3.29/ 7.44	7.33/ 7.44	60	0.33/0.71	Similar to assemblage above Sand bed 7		
					0.27/0.36	Increase in brackish epipelic diatoms: *A. coffeaeformis, D. smithii, F. subsalina, R. brebissonii.*	Q9-2/ Q13-2	Subsidence
9/13	**Sand bed 7**	2.18/ 3.00	3/ 2.99	18	–	Mixed assemblage: *A. coffeaeformis, K. oblongella, N. cari, N. cincta, O. pacifica, P. sulcata, P. intermedia, R. brebissonii, T. angulata.* Also contains anomalous marine tychoplanktonic diatom *D. Kippae* and *D. surirella* (<2% abundance).	–	
9/13	Brown, poorly sorted organic very fine sand/Brown, poorly sorted organic silt	3.01/ 5.09	5.43/ 5.09	70	1.4/1.29	Major freshwater diatoms: *C. pusilla, D. psuedovalis, E. praerupta, N. frustulum, P. intermedia C. pusilla.* Minor brackish diatoms: *A. coffeaeformis, D. psuedovalis, N. cincta, P. brevistriata, T. levidensis.*	Q9-1/ Q13-1	

* When data for both pits are available, they are reported with a dash separating the values. Diatom results are combined for each site.
[a] Mean grain size of sand beds and underlying and overlying sediment.
[b] Dominant grain size values for the 10th (D10) percentile (diameter at which 10% of the sample volume comprises smaller particles).
[c] LOI is a proxy for the percentage of organic matter in our fossil samples.
[d] Summary of diatom results used for interpreting coseismic land-level change. Full counts included in Figs. 6, 9, Figs. A1 and A4.
[e] Diatom zones determined by using a stratigraphically constrained incremental sum-of-squares (CONISS) cluster analysis (Figs. 6, 9, Figs. A1 and A4).
[f] Inferred land-level change based on grain size, LOI, and diatom analyses.

Table 5
Modeled ages for sand beds 6, 7, 8, and 9 at Tirúa and earthquake slip distribution.

Section(s)	Sand bed	Modeled age (AD)[a]	Modeled age range	Inferred land-level change (AD)[b]	Inferred slip distribution and rupture location (AD)[c]
T16	6	1520 ± 50	1470–1570	uplift	Deep, landward slip on the Maule segment
T16, Q9, Q13	7	1440 ± 15	1425–1455	subsidence	Shallow, offhosre slip on the Valdivia segment
T16	8	340 ± 70	270–410	uplift	Deep, landward slip on the Maule segment

[a] We used maximum and minimum limiting radiocarbon ages to calculate age probability distributions for inferred prehistoric tsunami beds from Tirúa section T16 with a bespoke Bayesian chronology model described in Appendix 1.
[b] Land-level change inferred from diatom based RSL reconstructions.
[c] Slip distribution and rupture location inferred from prehistoric land-level change and historical earthquake patterns.

diatoms (Figs. 5, 6 and 9, Figs. A3 and A6). Constrained cluster and DCA analyses reflect the shift in diatom species composition from the brackish and marine dominated samples below sand bed 4 to the freshwater and brackish dominated samples above the sand bed (Figs. 7, 8 and 10, Figs. A1, A2, A4, A5).

Radiocarbon dating from Ely et al. (2014) and Hong et al. (2017) constrains the age of sand bed 4 with maximum limiting ages of 1460–1640 AD and 1650–1800 and a minimum limiting age of 1640–1800 AD (Fig. 5b, 6a; Ely et al., 2014; Hong et al., 2017).

3.1.6. Sand bed 3 (Quidico)

A gray-brown, poorly sorted organic interbedded sand and silt (Q9), or a brown, poorly sorted organic silt (Q13) underlies sand bed 3 at Quidico (Fig. 6). Marine epipelic, epipsammic, and planktonic taxa increase in abundance in sediments immediately underlying sand bed 3 (Fig. 10, Fig. A4; Tables 3 and 4). Constrained cluster and DCA analyses reflect a shift in diatom species composition from freshwater and brackish dominated samples immediately above sand bed 4 at Quidico to marine and brackish dominated samples immediately below sand bed 3 (Fig. 8b and Fig. A5).

A sharp contact separates a clean, gray, well-sorted fine sand

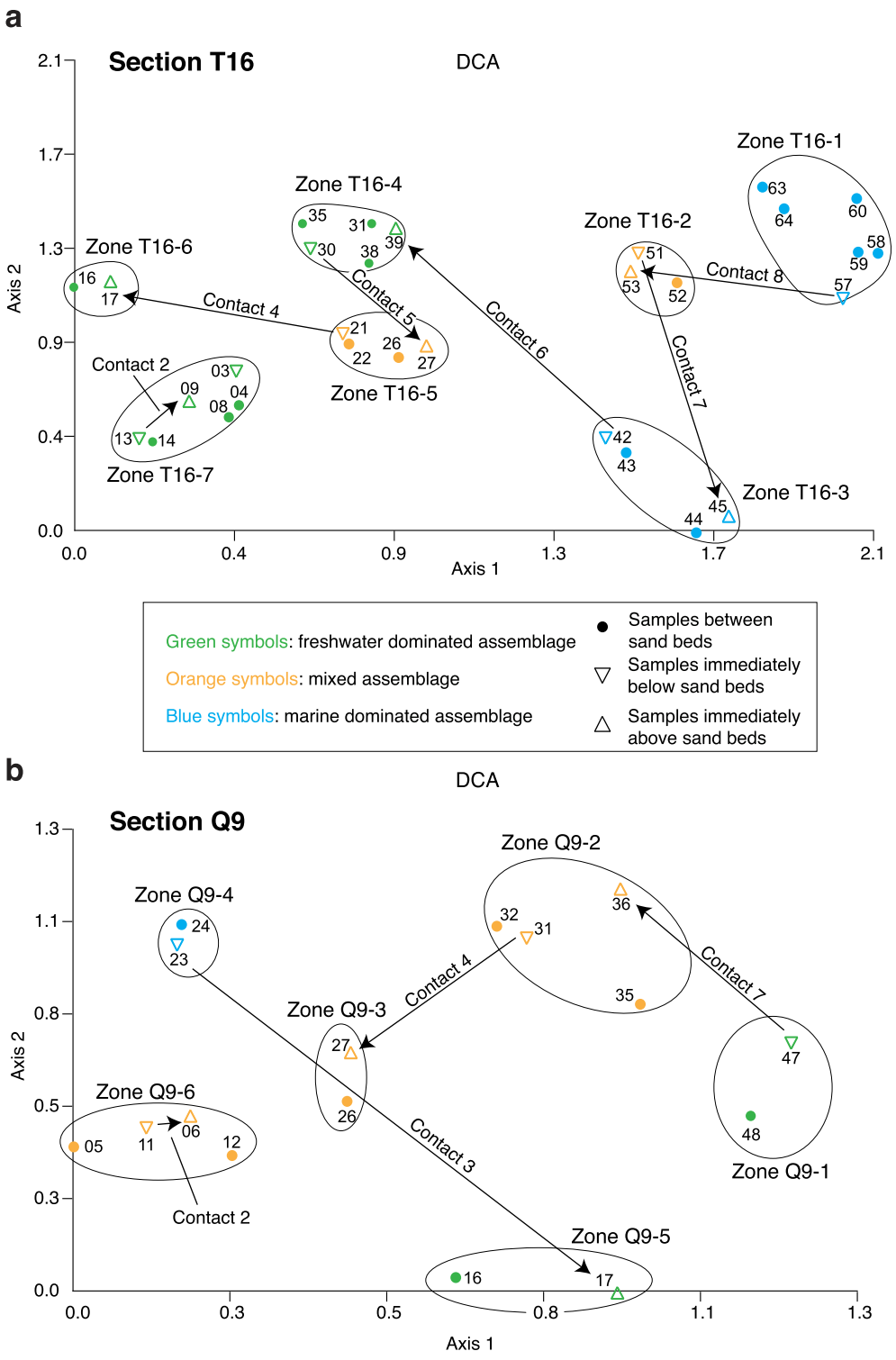

Fig. 8. Results of detrended correspondence analysis (DCA) for diatom samples from sections T16 (a) and Q9 (b). Samples with similar species compositions are grouped together in the DCA bi-plot and samples with statistically different species compositions plot apart (Horton et al., 2007). Paleoecological zones identified by the cluster analysis are labeled on the DCA bi-plot. Arrows show how assemblage bi-plot scores change from below to above labeled sand bed contacts.

(sand bed 3) from the underlying organic sand/silt. Sand bed 3 displays an increase in mean grain size and a decreased fine fraction (D10) and organic content (LOI; Fig. 6). The sand bed contains a mixed diatom assemblage composed of marine, brackish, and freshwater taxa at Quidico (Fig. 10 and Fig. A4). Notably, a low abundance (~3%) of the marine tychoplanktonic diatom *D. surirella*, not found in underlying or overlying sediment, was found in section Q13 (Fig. A4).

A brown, poorly sorted organic very fine sand (Q9) or a brown, poorly sorted organic silt (Q13) overlies sand bed 3. The organic sand/silt contains an increase in freshwater epipelic and tychoplanktonic taxa compared to the marine and brackish dominated

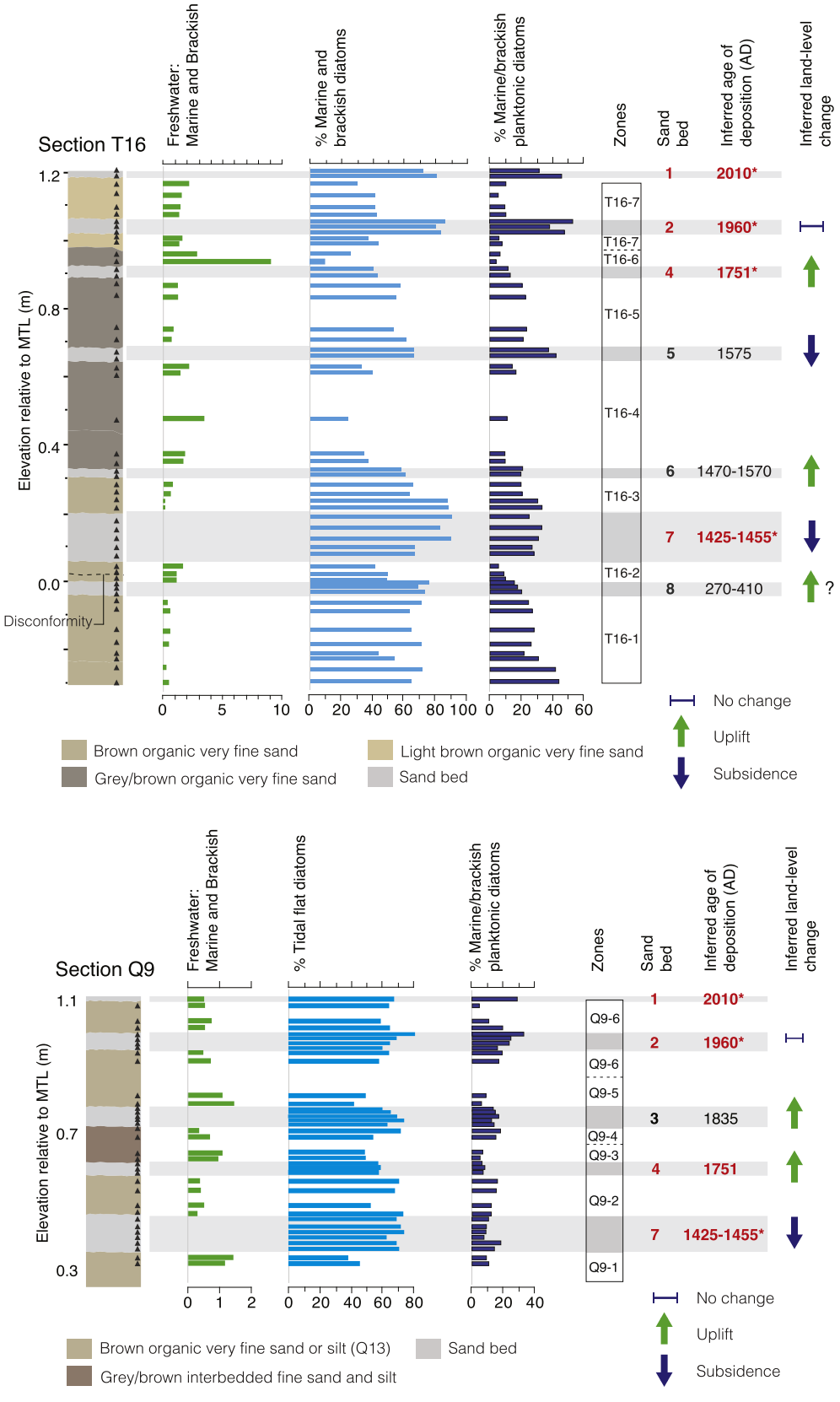

Fig. 9. Summary of evidence for land-level change and tsunami inundation for Tirúa section T16 and Quidico section Q9. Sand beds that correlate between sites are shown in red and by an asterisk on their inferred age. The ratio of freshwater to marine diatoms, the % marine and brackish diatoms, and the % marine/brackish planktonic diatoms is shown for samples above and below sand beds to highlight the change in assemblages across the beds. A decrease in the ratio of freshwater to marine diatoms and an increase in the % of marine and brackish diatoms and the % marine/brackish planktonic diatoms signals coseismic subsidence, while an increase in the ratio of freshwater to marine diatoms and an decrease in the % of marine and brackish diatoms and the % marine/brackish planktonic diatoms signals coseismic uplift. The % of marine and brackish diatoms and the % marine/brackish planktonic diatoms is shown for samples within sand beds. Evidence for tsunami inundation includes the high relative abundance of tidal flat diatoms within sand beds and the presence of marine planktonic diatoms within sand beds. Inferred coseismic land-level change and timing of coseismic land-level and sand bed deposition are shown for each event. (For interpretation of the references to colour in this figure legend, the reader is referred to the web version of this article.)

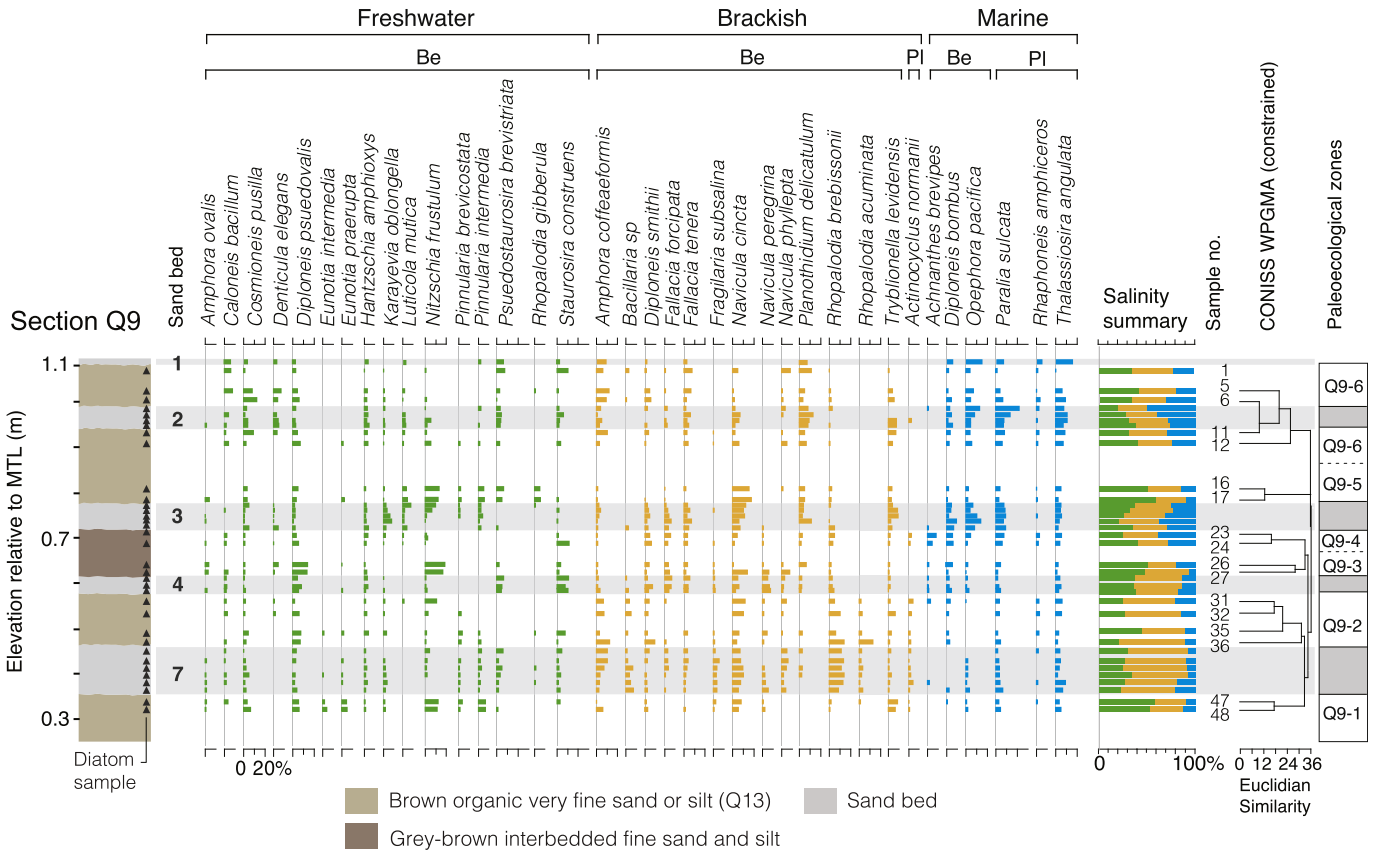

Fig. 10. Relative abundance of diatoms (showing only those species >5% abundance) for section Q9. Relative abundance is expressed as a percent of the total count. Triangle symbols on stratigraphic column show locations of numbered samples (sample numbers shown to the right of the salinity summary). The results of the stratigraphically constrained incremental sum-of-squares (CONISS) cluster analysis are shown beside our interpretation of paleoecological zones. Be: benthic; Pl: planktonic.

assemblage underlying sand bed 3. The decreased marine influence in reflected by an increase in LOI and the ratio of freshwater to marine and brackish diatoms, and a decrease in the percentage of marine and brackish planktonic diatoms (Figs. 6, 9, Fig. A6). Constrained cluster and DCA analyses reflect the shift in diatom species composition from the marine and brackish dominated samples below sand bed 3 to the freshwater and brackish dominated samples sand bed 3 (Fig. 8b and Fig. A5).

Radiocarbon dating below sand bed 3 yield a post-17th century age for sand deposition (Fig. 6b; Table 2; Hong et al., 2017).

3.1.7. *Sand bed 2 (Tirúa and Quidico)*

A light brown (T16 and T2), or brown (Q9 and Q13), poorly sorted organic very fine sand (T16, T2, Q9) or silt (Q13) underlies sand bed 2 (Figs. 5 and 6). Brackish epipelic and marine planktonic taxa increase in abundance in the organic sand/silt underlying sand bed 2 at Tirúa and Quidico (Figs. 7, 10, Figs. A1, A4; Tables 3 and 4). Constrained cluster and DCA analyses reflect a shift in diatom species composition from freshwater and brackish dominated samples immediately above sand bed 3 to marine and brackish dominated samples immediately below sand bed 2 (Figs. 7, 8 and 10, Figs. A1, A2, A4, A5).

A sharp contact separates a clean, gray, well-sorted fine sand (sand bed 2) from the underlying organic sand/silt. Sand bed 2 displays an increase in mean grain size and a decreased fine fraction (D10) and organic content (LOI; Figs. 5 and 6). The sand bed contains a mixed diatom assemblage composed of marine, brackish, and freshwater taxa, with a distinctive increase in marine epipsammic and planktonic taxa at Tirúa, and marine planktonic taxa at Quidico compared to underlying sediment (Fig. 9, Figs. A3, A6). In section Q13 at Quidico, sand bed 2 also contains anomalous marine tychoplanktonic diatoms not found in underlying or overlying sediment (Fig. A4).

A light brown (T16 and T2) or brown (Q9 and Q13), poorly sorted organic very fine sand (T16, T2, and Q9) or silt (Q13) overlies sand bed 2. The organic sand/silt contains a similar diatom assemblage to the organic sand/silt below sand bed 2 at both Tirúa and Quidico. Constrained cluster and DCA analyses reflect the similarity in diatom species composition of samples underlying and overlying sand bed 2 (Fig. 8, Figs. A2, A5).

In sections T2 and Q13, the presence of ^{137}Cs immediately below sand bed 2 places its age after AD ~1950 (Figs. 5 and 6; Ely et al., 1992, 2014; Cisternas et al., 2001; Hong et al., 2017).

3.1.8. *Sand bed 1 (Tirúa and Quidico)*

A light brown (T16 and T2) or brown (Q9 and Q13), poorly sorted organic very fine sand (T16, T2, and Q9) or silt (Q13) underlies sand bed 1 (Figs. 5 and 6a). Freshwater and brackish epipelic, and marine planktonic taxa dominate the assemblage in sediments underlying sand bed 1 at Tirúa and Quidico (Figs. 7, 10, Figs. A1, A4; Tables 3 and 4).

A sharp contact separates a clean, gray, well-sorted fine sand (sand bed 1) from the underlying organic sand/silt. Sand bed 1 displays an increase in mean grain size and a decreased fine fraction (D10) and organic content (LOI; Figs. 5 and 6a). The sand bed contains a mixed diatom assemblage composed of marine, brackish, and freshwater taxa, with a distinctive increase in marine epipsammic and planktonic taxa at Tirúa and Quidico compared to

underlying sediments (Fig. 9 and Fig. A3). Sand bed 1 was deposited by the tsunami that struck both Tirúa and Quidico on 27 February 2010 (Ely et al., 2014; Hong et al., 2017).

4. Discussion

At Tirúa and Quidico, we infer that the unusually abrupt, long lasting, and widespread changes in diatom assemblages we observe between units underlying and overlying the eight sand beds signal sudden decimeter-scale coseismic uplift and subsidence of the Tirúa and Quidico estuaries, in some cases followed by interseismic recovery. Such stratigraphic evidence of sudden RSL falls or rises—supported by diatom analyses—signaling coseismic uplift or subsidence has provided valuable insight into the long-term earthquake history of many subduction zones (e.g., Dura et al., 2016b). To help rule out gradual, localized, or short-term RSL changes and infer a coseismic origin for sharp stratigraphic contacts within coastal sedimentary sequences, the following criteria have been suggested: (1) presence of tsunami deposited sediments directly above sharp contacts (2) suddenness and persistence of RSL change (supported by microfossil evidence) associated with sharp contacts, replicated at each site; (3) lateral continuity of sharp stratigraphic contacts; (4) direction of land-level change (supported by microfossil evidence) across contacts, replicated at each site; and (5) synchronicity of contacts among sites (e.g., Nelson et al., 1996; Shennan et al., 2016).

4.1. New evidence for tsunami deposition

New grain size and LOI results from sections T16, T2, Q9, and Q13 show the sedimentology of the older sand beds in the sections is very similar to that of sand beds 1 and 2, deposited by historical tsunamis in 1960 AD and 2010. Sand beds 1 and 2 are composed of well-sorted fine sand (mean grain size = 2.20 Φ) and display a low fine fraction (mean D10 = 3.38 Φ) and low organic content (mean LOI = 3%; Figs. 5 and 6; Tables 3 and 4). Sand beds 3–8 are similarly composed of fine sand (mean grain size = 2.26 Φ), and display a low fine fraction (mean D10 = 3.45 Φ) and low organic content (mean LOI = 3%).

Diatom assemblages also support a tsunami source for the sand beds at Tirúa and Quidico (Figs. 7, 10, Figs. A1, A4). Within the mixed freshwater, brackish, and marine diatom assemblages that typically characterize tsunami deposits (e.g., Dawson et al., 1996; Dawson and Smith, 2000; Smith et al., 2004; Bondevik et al., 2005; Sawai et al., 2008, 2009; Horton et al., 2011; Nelson et al., 2015), sand beds 1 and 2 display high relative abundances of marine planktonic (e.g., *Paralia sulcata*, *Thalassiosira angulata*), tychoplanktonic (*Delphineis kippae* and *D. surirella*), and epipsammic (*Opephora pacifica*) diatoms common in the Quidico coastal littoral zone (Hong et al., 2017). Similar increases in marine planktonic, tychoplaktonic, and epipsammic diatoms are observed in sand beds 3, 5, and 7, supporting an offshore source rather than a fluvial source for the sand beds. Because marine conditions preceded the deposition of sand beds 4, 6, and 8, the percentage of marine diatoms in the sand beds does not stand out from underlying sediments; however, the marine dominated assemblage in the sand beds is distinct from overlying sediments.

4.2. Evidence for coseismic land-level change

The diatom assemblages in units overlying sand beds 3–8 show an abrupt shift in the marsh environment consistent with sudden RSL change from coseismic deformation, rather than a gradual response to long-term RSL change. A sudden increase in freshwater diatoms in units overlying sand beds 3 and 4 (described at Tirúa and Quidico) and 6 and 8 (described only at Tirúa) is consistent with coseismic uplift (Fig. 9). Sediment underlying the sand beds contains higher abundances of marine epipsammic (*O. pacifica*), planktonic (*P. sulcata, T. angulata*), and brackish epipelic (e.g., *Navicula cincta, Diploneis smithii, Rhopalodia brebissonii*) diatoms than overlying sediment, which displays a lasting increase in freshwater taxa (*Diploneis psuedovalis, H. amphioxys, K. oblongella, Nitzschia frustulum, Pinnularia intermedia*) and a significant decrease in marine planktonic diatoms (Figs. 7 and 10). An increase in LOI, indicative of reduced tidal inundation and increased marsh vegetation, and uplift of the lowland, was also measured in sediment overlying sand beds 3, 4, 6, and 8 (Figs. 5 and 6; e.g., Nelson et al., 1996; Witter et al., 2003). A sudden increase in the abundance of marine and brackish diatoms in units overlying sand beds 5 (only described at Tirúa) and 7 (described at Tirúa and Quidico) is consistent with coseismic subsidence (Figs. 7 and 10). Diatom assemblages in sediment underlying the sand beds contain abundant freshwater taxa (e.g., *D. psuedovalis, K. oblongella, N. frustulum, P. intermedia*), while sediment overlying the sand bed displays a lasting increase in brackish epipelic (e.g., *Amphora coffeaeformis, D. smithii, Fragilaria subsalina*) and marine epiphytic (e.g., *Achnanthes brevipes*), planktonic (e.g., *P. sulcata, T. angulata*), and epipsammic (e.g., *O. pacifica*) taxa. A decrease in LOI, indicative of increased tidal inundation and decreased marsh vegetation, and hence subsidence of the lowland, was also measured in sediment overlying sand beds 5, and 7 (Figs. 5 and 6; e.g., Shennan et al., 2009).

The diatom assemblages in units overlying sand beds 3–8 display a lasting shift in the marsh environment, rather than a temporary response to short-term sea-level fluctuations (e.g., El Niño events, storms; Witter et al., 2001) or fluvial inundation (Hemphill-Haley, 1995). In addition, above sand bed 4 at Tirúa, and sand beds 3 and 4 at Quidico, the influx of freshwater species in the units overlying sand beds is followed by a gradual increase in marine and brackish taxa, suggesting gradual interseismic subsidence of the marsh (Figs. 7 and 10). Although not as pronounced, the influx of marine and brackish diatoms above sand beds 5 and 7 at Tirúa is followed by an increase in freshwater taxa, suggesting gradual interseismic uplift of the marsh (Figs. 7 and 10).

At Tirúa and Quidico, the RSL changes spanning the sand beds were correlated over the ~130 m separating sections T16 and T2, and the ~150 m separating sections Q9 and Q13. In addition, the direction of land-level change spanning sand beds preserved at both sites (sand beds 1, 2, 4, and 7) is consistent. Our qualitative interpretations of changes (or lack of changes) in diatom species composition in sediments underlying and overlying the sand beds are supported by cluster analysis and DCA results (Figs. 7, 8 and 10, Figs. A1, A2, A4, A5) that show shifts in marsh environments (e.g., brackish to freshwater conditions), which in the local tidal regime translate to decimeter-scale coseismic land-level change across sand beds. The inter-site and intra-site continuity of the LOI and diatom evidence for sudden coseismic land-level change coincident with sand bed deposition at Tirúa and Quidico helps rule out localized processes and gradual RSL change as a mechanism for the environmental shifts associated with the sand beds (Figs. 3a, 9; Hemphill-Haley, 1995). Environmental changes spanning sand bed 8 were only described in section T16, however the LOI and diatoms overlying the sand bed display similar ecological changes to those observed above widely correlated sand beds (Figs. 7 and 9).

Tirúa and Quidico are only 10 km apart, so we would expect that both would experience the same direction of coseismic land-level change in a given earthquake. Based on our diatom results, the radiocarbon ages of the sediments, and the historical sequence of earthquakes with sources to the north or south, the previous geochronology and correlations of Ely et al. (2014) and Hong et al. (2017) remain the most consistent with all data. All correlated

sand beds between the sites showed the same direction of coseismic land-level change. The sand beds attributed to historical ruptures on the Maule segment to the north (sand beds 1, 3 and 4) showed evidence of coseismic uplift, and those attributed to historical ruptures on the Valdivia segment to the south (sand beds 2 and 5) showed no change or coseismic subsidence. In those cases in which tsunami sand beds were identified at one site and not the other, we conclude that inundation from those tsunamis was either not as great at the second site, or the deposit was too thin or patchy to be well preserved throughout the second site and was not apparent in our stratigraphic sections. The diatom results increased our confidence in the stratigraphic correlations between Tirúa and Quidico for the period of the historical record. We therefore employed the same process to correlate the prehistoric deposits (6–8) between the two sites.

4.3. Inferred slip distributions for earthquakes

The geometry of the megathrust fault plane and the amount and distribution of down-dip and along-strike coseismic and interseismic slip on the fault control the vertical displacement of coastlines above subduction zones. Because the distribution of coseismic slip can vary among earthquakes, one coastal location may record a mixed uplift and subsidence record (Plafker, 1965; Plafker and Savage, 1970; Wang et al., 2012; Briggs et al., 2014).

A simple coast-perpendicular coseismic slip model at Tirúa and Quidico demonstrates the potential for variable down-dip slip to produce a mixed uplift and subsidence record at our sites (Fig. 11). The model indicates a deeper, landward distribution of slip will result in coseismic uplift at Tirúa and Quidico (Fig. 11a), while a shallower distribution of slip concentrated offshore will result in coseismic subsidence (Fig. 11c; Moreno et al., 2009, 2012; Ely et al., 2014). Slip at an intermediate depth will produce a hinge line between coseismic uplift and subsidence (i.e., zero net land-level change) at or near Tirúa and Quidico (Fig. 11d), while a wide rupture with combined deep and shallow slip will produce slight uplift (Fig. 11b).

A coast-parallel slip model at Tirúa and Quidico also demonstrates the potential for mixed uplift and subsidence records at the lateral ends of ruptures (e.g., Briggs et al., 2014); subsidence troughs may wrap around the edges of uplift zones and uplift zones may wrap around the edges of subsidence troughs.

Historically, ruptures on the Maule portion of the subduction zone (e.g., 2010 AD; 1835, 1751) have produced coastal uplift, suggesting deep or wide, landward slip on the megathrust, and ruptures on the Valdivia portion of the subduction zone (e.g., 1960 AD, 1575) have produced coastal subsidence or no net land-level change, indicating shallow to intermediate, offshore slip on the megathrust. The recent, well-documented coastal uplift observed at Tirúa and points north following the 2010 M_w 8.8 earthquake is consistent with deep, landward slip at the Arauco Peninsula inferred from slip distribution models for the event (Moreno et al., 2012), while the little to no detectable land-level change at our sites and subsidence at points south observed following the 1960 earthquake sequence is consistent with inferred intermediate to shallow, offshore slip on the megathrust (e.g., Plafker and Savage, 1970; Moreno et al., 2009; Garrett et al., 2013; Ely et al., 2014).

Thus, based on historical deformation patterns and our modeling results, we infer that uplift at our sites is likely produced by deep or wide, landward slip on the Maule portion of the subduction zone, while no net land-level change or subsidence is likely produced by shallow to intermediate, offshore slip on the Valdivia portion of the subduction zone. We also consider the possibility of small, localized ruptures with significant coastal deformation, and coast-parallel slip variability at the lateral ends of ruptures causing uplift or subsidence at our sites, especially for earthquake evidence that we were not able to correlate widely along the subduction zone (e.g., sand beds 8 and 6). We infer that past ruptures resulting in uplift at our sites are reflected in the coastal stratigraphy by an abrupt increase in LOI and the ratio of freshwater to marine and brackish diatoms (Fig. 11e), while coseismic subsidence results in a decrease in LOI and the ratio of freshwater to marine and brackish diatoms (Fig. 11f).

4.3.1. Prehistoric earthquake: 340 AD ± 70 (sand bed 8)

An increase in LOI and freshwater diatoms above sand bed 8 at Tirúa is consistent with coseismic uplift (i.e. RSL fall) coincident with sand deposition (Fig. 11e). However, the disconformity observed above sand bed 8 suggests that the environmental change may be the result of the time gap and possible erosion of sediments above the sand bed. The modeled age range of sand bed 8 (270–410 AD; Fig. 4; Table 5) at Tirúa overlaps with age estimates for stratigraphic evidence of coseismic subsidence about 250–650 AD at Valdivia (Nelson et al., 2009), an extensive lacustrine turbidite in 270–290 AD described by Moernaut et al. (2007) in Lago Puyehue, 100 km southeast of Valdivia, and coastal lacustrine evidence of tsunami inundation at Lake Huelde in 165–350 AD (Fig. 12). However, diatom evidence of coseismic uplift associated with sand bed 8 is inconsistent with a rupture on the Valdivia portion of the subduction zone similar to that implied by the widespread earthquake and tsunami evidence in the Valdivia region. Because of the disconformity above sand bed 8 and the lack of correlative evidence of a rupture on the Maule portion of the subduction zone when sand bed 8 was deposited, we cannot confidently attribute the paleoenvironmental change above sand bed 8 to coseismic uplift rather than channel migration or some other process of environmental change. However, the sedimentology of sand bed 8 is consistent with tsunami deposition during this time period.

4.3.2. Prehistoric earthquake: 1440 AD ± 15 (sand bed 7)

The pronounced decrease in LOI and increase in brackish and marine planktonic diatoms above sand bed 7 at Tirúa and Quidico is indicative of coseismic subsidence (i.e. RSL rise), which we infer was the result of shallow, offshore slip along the Valdivia portion of the subduction zone (Fig. 11c, f). A maximum age (1440–1490 AD) from below sand bed 7 and minimum age (1450–1620 AD) from above sand bed 6 constrain the timing of sand bed 7 deposition at Tirúa. An age model at Quidico constrains that age of the sand bed to between 1445 and 1490 AD (Hong et al., 2017). Because of the overlapping age ranges of the sand bed, and because evidence for coseismic subsidence was observed at both Tirúa and Quidico coincident with sand bed deposition, we correlated sand bed 7 between sites. The combined maximum and minimum ages at Tirúa and Quidico result in a modeled age of 1425–1455 AD for sand bed 7 deposition (Fig. 4; Table 5).

There are at least two possible correlations and interpretations of the extent of the event that deposited sand bed 7. First, widespread evidence of a large earthquake and tsunami in southern Chile around this time period exists in the form of lacustrine turbidite records in Lago Calafquén and Lago Riñihue (1310–1327 AD; Moernaut et al., 2014), coseismic subsidence and tsunami inundation at the Maullín River estuary (1280–1387 AD; 41.6° S; Cisternas et al., 2005) and Chucalén (1270–1450 AD; 41.8° S; Garrett et al., 2015), stratigraphic evidence of shaking and tsunami inundation at Cocotue (1300–1398 AD; 41.9° S; Cisternas et al., 2017a), and coastal lacustrine evidence of tsunami inundation at Lake Huelde (1280–1397 AD; 42.6° S; Kempf et al., 2017) (Fig. 12). Our evidence of coseismic subsidence between 1425 and 1455 is consistent with the shallow, offshore slip typical of Valdivia ruptures, supporting a correlation with the earthquake along the

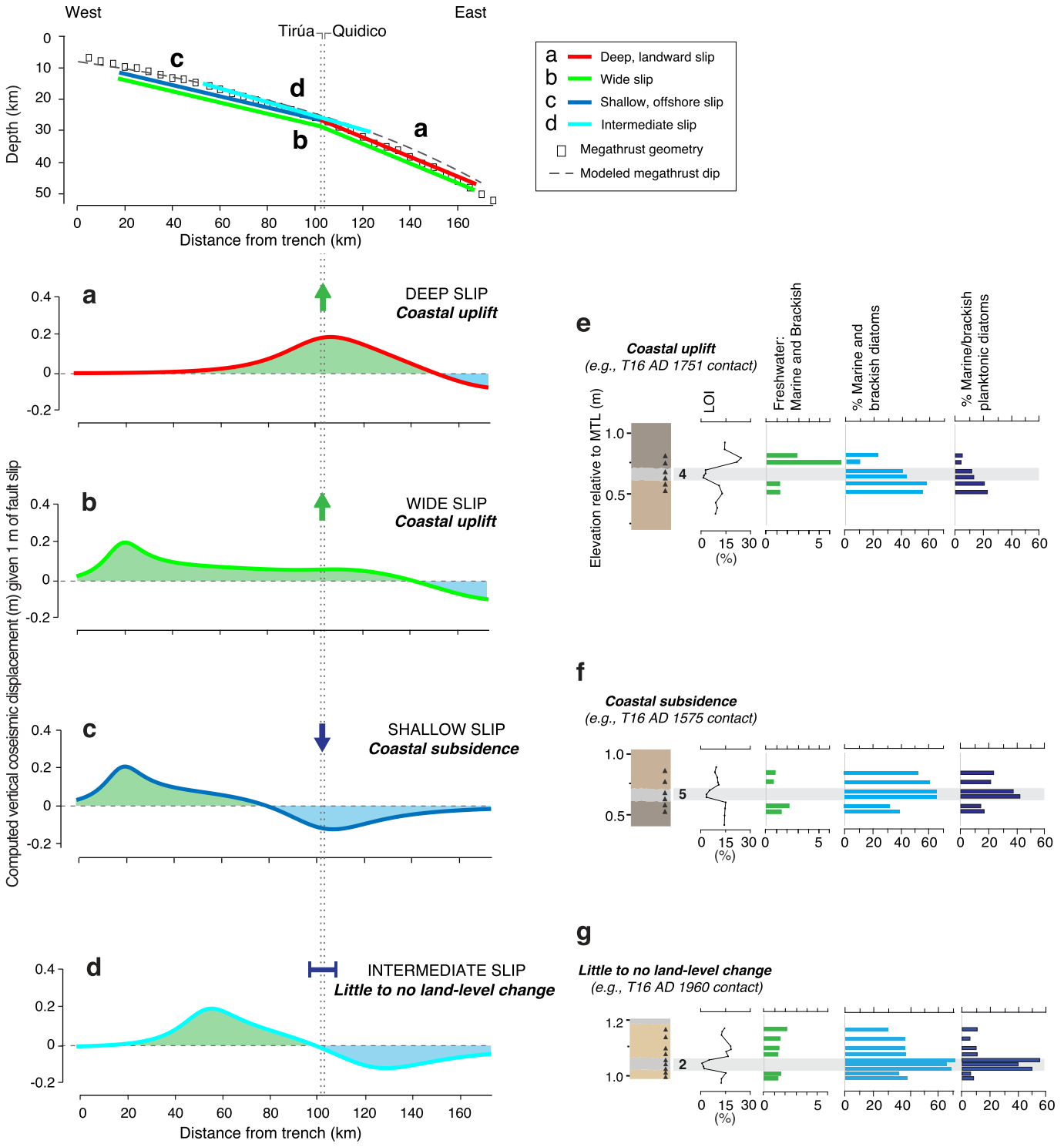

Fig. 11. A simple model of constant coseismic slip and corresponding vertical deformation on a subduction zone megathrust in which slip is confined to (a) a deep (25–45 km) zone; (b) a wide (10–45 km) zone; (c) a shallow (10–25 km) zone; (d) an intermediate (15–30 km) zone. e) An example of the LOI and diatom response to coastal uplift (sand bed 4 and underlying and overlying sediment) produced by a deep slip zone entirely landward of the sites or a wide slip zone. f) An example of the LOI and diatom response to coastal subsidence (sand bed 5 and underlying and overlying sediment) produced by a shallow slip zone entirely offshore of the sites. g) An example of the LOI and diatom response to little to no land-level change (sand bed 2 and underlying and overlying sediments) produced by a intermediate slip zone beneath the sites. The megathrust geometry is modeled as a plane dipping 15.5°. For comparison, the megathrust geometry of Moreno et al. (2012) is shown by the small rectangles in the top panel. Figure and caption are modified from Ely et al. (2014).

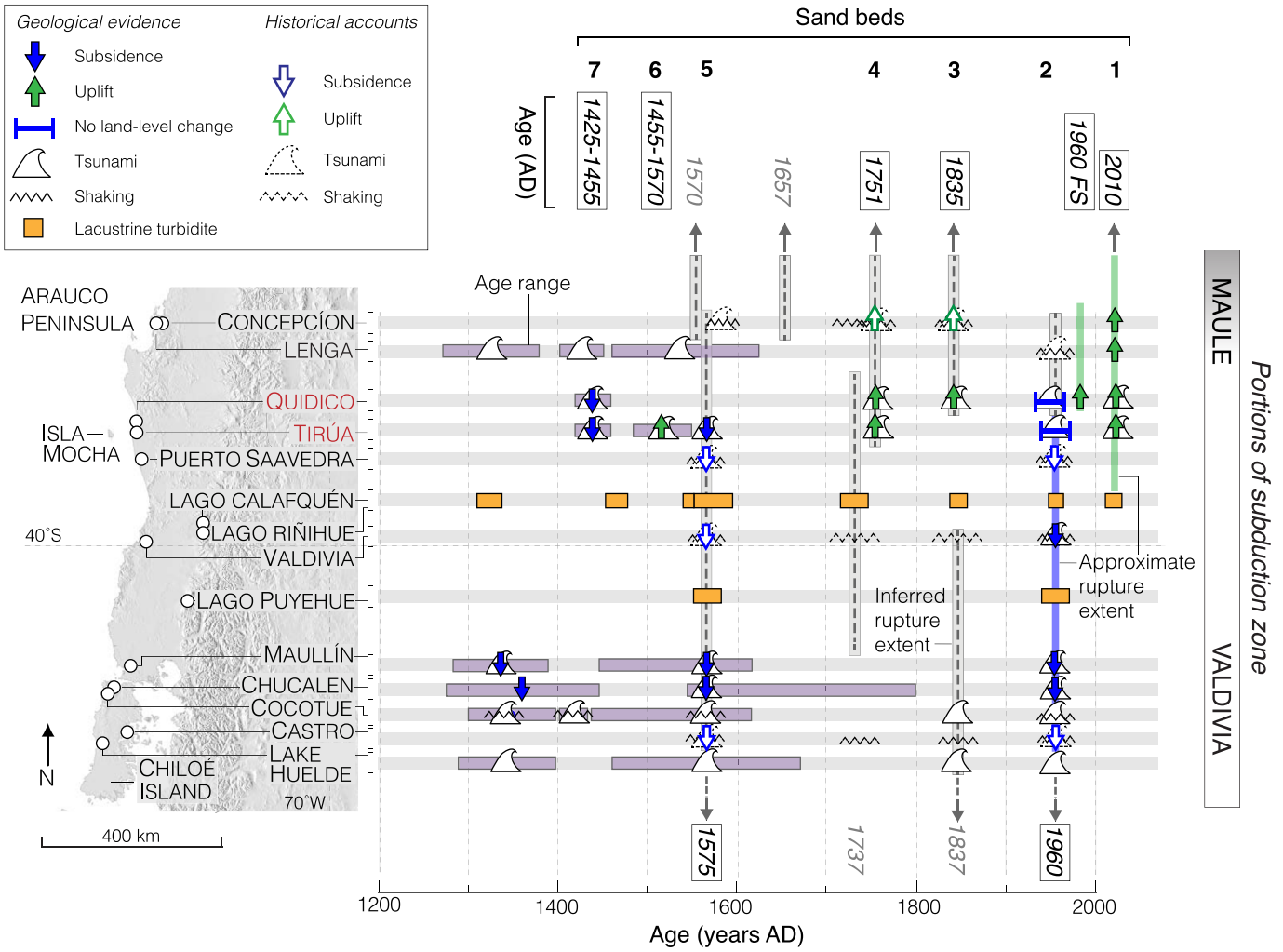

Fig. 12. Summary of historical and palaeoseismic evidence for great ruptures along the Valdivia and Maule portions of the subduction zone over the last ~800 years. Historical records summarized by Lomnitz (1970), Cisternas et al. (2005, 2017a, b), and Udías et al. (2012); stratigraphic and biostratigraphic evidence from Cisternas et al. (2005, 2017a, b), Nelson et al. (2009), Garrett et al. (2013, 2015); Ely et al. (2014), Moernaut et al. (2007, 2014), Kempf et al. (2017). FS: 1960 Foreshock.

Valdivia portion of the subduction zone described in Moernaut et al. (2014), Cisternas et al. (2005, 2017a), Garrett et al. (2015), and Kempf et al. (2017) (Fig. 11c, f). Cisternas et al. (2017a) characterize this widespread earthquake evidence as an 1837-style rupture on the Valdivia portion of the subduction zone. However, our new evidence of coseismic subsidence during this time period as far north as Tirúa and Quidico suggests that the 1425–1455 rupture may have exceeded the size of an 1837-style rupture. We did not observe evidence of the 1837 earthquake or tsunami at our sites, and while Lago Calafquén and Lago Riñihue record evidence of shaking in 1837, there are no historical accounts or geologic records of land-level change or tsunami inundation north of Maullín associated with the 1837 AD rupture. Second, it is possible that the evidence of coseismic subsidence and tsunami inundation at Tirúa and Quidico between 1425 AD and 1455 is the result of a separate rupture along the northern end of the Valdivia portion of the subduction zone during this time period. In this scenario, our evidence for subsidence and tsunami inundation may correlate with lacustrine turbidite evidence of shaking in Lago Calafquén and Lago Riñihue between 1460 AD and 1470 (Moernaut et al., 2014).

4.3.3. Prehistoric earthquake: 1520 AD ± 50 (sand bed 6)

The abrupt increase in LOI and freshwater diatoms above sand bed 6 at Tirúa is indicative of coseismic uplift (i.e. RSL fall), which we infer was the result of deep, landward slip along the Maule portion of the subduction zone (Fig. 11a, e). The modeled age for sand bed 6 deposition is 1470–1570 AD (Fig. 4; Table 5). Lacustrine turbidite records in Lago Calafquén northeast of Valdivia contain an event during this time period (1544–1548 AD; Moernaut et al., 2014) that has been correlated to sedimentary evidence of shaking and tsunami inundation on Chiloé Island between 1505 AD and 1802 (Cisternas et al., 2017a). This evidence of shaking and tsunami inundation to the south of Tirúa suggests that this rupture occurred on the Valdivia portion of the subduction zone. Cisternas et al. (2017a) attribute their sedimentary evidence of shaking and tsunami inundation to an 1837-style rupture. However, the shallow, offshore slip that characterizes ruptures on the Valdivia portion of the subduction zone have historically produced subsidence at our sites, and we observed uplift coincident with the deposition of sand bed 6. Our evidence of uplift at Tirúa could point to a more northern, local source for the rupture. It could also indicate that the site was located on the lateral end of an intermediate or shallow, offshore rupture on the Valdivia portion of the subduction zone,

where a zone of uplift wrapped around a subsidence trough, as shown in Plafker (1972) and Cisternas et al. (2017b).

4.3.4. 1575 AD earthquake (sand bed 5)

The 1575 AD (M ~9.5) earthquake and tsunami are represented by evidence of coseismic subsidence and tsunami inundation (sand bed 5) at Tirúa. The abrupt decrease in LOI and increase in brackish and marine diatoms above sand bed 5 at Tirúa is indicative of coseismic subsidence (i.e. RSL rise), which we infer was the result of shallow, offshore slip along the Valdivia portion of the subduction zone (Fig. 11c, f). Our inferences are consistent with historical accounts of coseismic subsidence 50 km south of Tirúa at the mouth of the Imperial River near Puerto Saavedra and in Valdivia during the earthquake. Based on historical accounts and geologic evidence, the 1575 earthquake is thought to be similar in magnitude to the giant 1960 earthquake and was likely characterized by similar shallow, offshore slip (Figs. 11c and 12; Cisternas et al., 2005). Geologic studies describe evidence of shaking, coseismic subsidence, and/or tsunami inundation in both 1575 and 1960 at Lago Calafquén and Lago Riñihue (Moernaut et al., 2014), the Maullín River estuary (Cisternas et al., 2005), Chucalén (Garrett et al., 2015), Cocotue (Cisternas et al., 2017a), and Lago Huelde (Kempf et al., 2017) (Fig. 12).

We did not identify stratigraphic or diatom evidence of coseismic subsidence and tsunami inundation in 1575 at Quidico, which suggests that the rupture might not have reached as far north as the 1960 rupture. The subsidence we observed at Tirúa in 1575, where there was little or no change of land level in 1960, suggests that the slip may have been more concentrated offshore than it was in 1960, and that there was very little or no deeper slip on the megathrust similar to that experienced in 2010, 1835, and 1751. To explain the absence of a 1575 tsunami deposit in our stratigraphic sections at Quidico, Hong et al. (2017) suggested that the northward orientation of the Quidico embayment may favor the preservation of deposits from tsunamis generated by ruptures along the Maule portion of the subduction zone (Fig. 2b).

4.3.5. 1751 AD earthquake (sand bed 4)

The 1751 AD (M ~8.5) earthquake and tsunami are represented by evidence of coseismic uplift and tsunami inundation (sand bed 4) at Tirúa and Quidico. The pronounced increase in LOI (only at Tirúa) and freshwater diatoms above sand bed 4 at both sites is indicative of coseismic uplift (i.e. RSL fall), which we infer was the result of deep, landward slip along the Maule portion of the subduction zone (Fig. 11a, e). Our inferences are consistent with historical accounts of coseismic uplift north of our sites (e.g., in the Bay of Concepción) during the earthquake (Fig. 12; Lomnitz, 2004; Udías et al., 2012). The 1751 earthquake and tsunami were highly destructive—leading to the inland relocation of Concepción—and have been compared to the 2010 (M_w 8.8) Maule rupture and accompanying tsunami (Ely et al., 2014). The historical accounts of uplift around the Bay of Concepción in 1751, as well our diatom evidence for coseismic uplift at Tirúa and Quidico are consistent with this comparison, showing that the rupture extended at least as far south as 2010 (and farther than the 1835 rupture) and that the slip extended to sufficient depth to cause uplift at both of our sites (Fig. 11b; Moreno et al., 2012). The evidence for a large tsunami within the Bay of Concepción and at Quidico and Tirúa suggests that there was also a significant component of tsunamigenic offshore slip near our sites in 1751, similar to that during the 2010 rupture.

4.3.6. 1835 AD earthquake (sand bed 3)

The 1835 AD (M 8.0–8.5) earthquake and tsunami are represented by evidence of coseismic uplift and tsunami inundation (sand bed 3) at Quidico. The abrupt increase in LOI and freshwater diatoms above sand bed 3 is indicative of coseismic uplift (i.e. RSL fall) at Quidico in 1835, which we infer was the result of deep, landward slip along the Maule portion of the subduction zone (Fig. 11a, e). Our inferences are consistent with historical accounts of coseismic uplift north of Quidico (e.g., Tubul and Isla Santa María) during the earthquake (Fig. 12; FitzRoy, 1839; Darwin, 1839; Lomnitz, 2004; Wesson et al., 2015). In the cases of Tubul and Isla Santa María, historical accounts of uplift were much larger in 1835 than in 2010. However, south of the Arauco Peninsula, first and secondhand accounts of the 1835 earthquake in FitzRoy (1839) describe less uplift at Lebu and Isla Mocha than that observed in 2010, suggesting that the rupture was likely dying out in this region and did not extend as far south as the 1751 or 2010 (to be discussed below) ruptures. The absence of diatom evidence of coseismic uplift in our stratigraphic sections at Tirúa in 1835 is consistent with a southern termination of the rupture near our sites. To explain the presence of an 1835 tsunami deposit at Quidico but not Tirúa, Hong et al. (2017) proposed that the northward facing embayment at Quidico may result in the selective accumulation and preservation of tsunami deposits generated by ruptures on the Maule portion of the subduction zone (Fig. 2b).

4.3.7. 1960 AD earthquake (sand bed 2)

The 1960 earthquake and tsunami are represented by evidence for tsunami inundation (sand bed 2), but little to no coseismic land-level change at Tirúa and Quidico. The 1960 Valdivia earthquake sequence included a series of foreshocks (maximum M_w 8.2) offshore of the Arauco peninsula extending to ~39°S, which produced coastal uplift north of Tirúa and Quidico (Plafker and Savage, 1970), and a mainshock (M_w 9.5; Cifuentes, 1989, Fig. 1b) extending from the Arauco Peninsula to ~47°S, which produced widespread coastal subsidence south of Tirúa and Quidico (Plafker and Savage, 1970; Moreno et al., 2009). The inferred slip distribution during the mainshock is characterized by a shallow to intermediate slip zone concentrated offshore along the Valdivia portion of the subduction zone (Fig. 12; Moreno et al., 2009). Similar LOI and diatom assemblages underlying and overlying sand bed 2 suggest little or no net coseismic land-level change at Tirúa or Quidico associated with the 1960 earthquake sequence, consistent with a shallow to intermediate slip zone at our sites (Fig. 11d, g).

Our results from Tirúa are consistent with the diatom analysis of Garrett et al. (2013), the stratigraphic evidence documented by Ely et al. (2014), and the observations of Plafker and Savage (1970), who found little to no land-level change there following the 1960 earthquake sequence. Our results from Quidico, however, are inconsistent with the ~1.0 m of coseismic uplift documented near that site by Plafker and Savage (1970). Plafker and Savage (1970) based their large (~1.0 m) difference in uplift between the two sites, only ~10 km apart, on pre- and post-earthquake elevations of the lower growth limits of vegetation and resident accounts of changes in extreme high and low tides. The difference may be attributed to Tirúa's location on the southern edge of the foreshock uplift zone, where uplift rapidly diminished. Because the location of Plafker and Savage's (1970) Quidico report is unclear (the location differs on their Table 1 and Fig. 3), and our results suggest no land-level change at either site, uplift in 1960 may have been farther north, leaving both Tirúa and Quidico south of the foreshock uplift zone. The net deformation for the 1960 earthquake sequence depicted in Fig. 2 in Plafker and Savage (1970) shows both Tirúa and Quidico on the hinge line between uplift expected offshore and subsidence expected farther inland during the shallow to intermediate, offshore slip of the 1960 mainshock (Fig. 11d; Plafker and Savage, 1970; Moreno et al., 2009; Ely et al., 2014).

4.3.8. 2010 AD earthquake (sand bed 1)

The tsunami produced by the 2010 rupture is represented by sand bed 1 at Tirúa and Quidico. Surveys conducted at Tirúa one month before and weeks to one year following the 2010 Maule earthquake measured between 0.5 and 1.0 m of coseismic uplift (Farías et al., 2010; Melnick et al., 2012; Ely et al., 2014). Inferred slip distributions for the 2010 earthquake show that the coastal uplift was the result of deep, landward slip on the Maule portion of the subduction zone (Fig. 11a; Moreno et al., 2012; Wesson et al., 2015).

4.4. Interseismic land-level changes

Assuming classical elastic rebound (Reid, 1910; Segall, 2010), interseismic land-level change due to accumulation of elastic strain should follow coseismic land-level change, typically with a sign opposite to that of the coseismic change. For example, Wesson et al. (2015) measured about 1.5 m of shoreline interseismic subsidence at Isla Santa María in the Gulf of Arauco between coseismic uplift during earthquakes in 1835 AD and 2010. Interseismic land-level change could also be caused by periods of aseismic slip on portions of the megathrust or by earthquakes on deeper parts of the megathrust that produce less tsunami excitation (Cisternas et al. 2017b; Wang et al., 2007; Carvajal and Gubler, 2016).

With microfossil methods, long-term tectonic changes in land level over hundreds to thousands of years are more difficult to distinguish from other long-term environmental changes than are rapid coseismic changes. However, the gradual increase in marine and brackish taxa that followed evidence of coseismic uplift coincident with sands beds 3 and 4 at Quidico and sand bed 4 at Tirúa (1835 AD and 1751) is consistent with gradual interseismic subsidence of the marsh (Figs. 7 and 10). This pattern suggests that following a large megathrust earthquake with sufficient slip to cause a large tsunami and that includes slip extending to sufficient depth to uplift Quidico and Tirúa, interseismic strain accumulation would be expressed as subsidence, as was observed at these two sites following coseismic uplift in 1751 AD and 1835.

More intriguing are the periods of interseimic uplift observed at Tirúa following earthquakes characterized by subsidence in 1425–1455 AD and 1575. For example, the influx of marine and brackish diatoms above sand beds 5 and 7 at Tirúa is followed by an increase in freshwater taxa, suggesting gradual interseismic uplift of the marsh (Figs. 7 and 10). The coseismic subsidence during these two earthquakes was likely caused by shallow, offshore slip. A simple relocking of the megathrust from near the trench to significant depth following these events would not likely cause uplift, but rather subsidence. In contrast, the apparent interseismic uplift may be more likely caused by subsequent earthquakes too deep on the megathrust to cause tsunamis (Cisternas et al., 2017b, 1737 explanation), or perhaps by aseismic slip on the megathrust below the portion that slipped in the preceding shallow earthquake.

4.5. Length of record and recurrence intervals of earthquakes

The length of the earthquake and tsunami record at Tirúa (~1800 years) is comparable to coastal stratigraphic records near Maullín (Atwater et al., 1992; Cisternas et al., 2005) and Valdivia (Nelson et al., 2009), where coastal sedimentary sequences are underlain by distinct unconformities a few hundred to a few thousand years old. Above the unconformities at these two sites, Atwater et al. (1992) and Nelson et al. (2009) described reworked tidal and floodplain mud, peat, and sand with only fragmentary evidence of coseismic land-level change or tsunami inundation. Like our record at Tirúa and Quidico, Cisternas et al. (2005) described a more complete sequence of earthquakes and/or tsunamis, at Maullín, with evidence for eight events in the last 2000 years.

Atwater et al. (1992), Nelson et al. (2009), and Dura et al. (2015, 2016b) attribute the fragmentary nature of Chilean coastal paleoseismic records to net emergence (RSL fall) during the late Holocene that limited the accommodation space necessary for the aggradation of coastal marshes critical for the preservation of earthquake and tsunami evidence. Field evidence in south-central Chile and ICE-5G VM5a model predictions for the region suggest RSL fell from a high of 3–8 m in the mid-Holocene to its present level (e.g., Peltier, 2002, 2004; Isla et al., 2012; Roy and Peltier, 2015).

Our paleoenvironmental reconstructions along with previous geologic studies in the region indicate ~1 m of RSL fall in the last 1000–2000 years (Atwater et al., 1992; Bartsch-Winkler and Schmoll, 1993). The base of our oldest stratigraphic section at Tirúa (T16) contains a reworked tidal and floodplain organic silty sand containing leaves, stems, and logs and a greater percentage of brackish and marine diatoms, consistent with higher RSL at the site ~1800 years ago. A disconformity separates this more brackish and marine basal unit from the overlying brackish-fresh units that host our earthquake and tsunami records. Within the continuous sedimentary sequence above the disconformity, diatoms show little to no net RSL change in the last ~600 years.

Based on our evidence for seven instances of coseismic land-level change and tsunami inundation preserved at Tirúa and Quidico in the last ~600 years, the recurrence interval of large ($M > 8$), near-source tsunamigenic earthquakes ranges from 50 to 180 years, with an average recurrence interval of ~100 years (Fig. 12). A 100-year recurrence interval is consistent with the historical recurrence of destructive ($M > 8$) earthquakes and tsunamis along the Maule portion of the subduction zone (Lomnitz, 2004), although our records do not contain two of the ruptures (1570 AD and 1657) used to calculate the historical interval. Instead, the 100-year interval between earthquakes at our sites probably reflects their location in the area where ruptures generated on the Maule and Valdivia portions of the subduction zone overlap, allowing evidence of deformation during northern and southern earthquakes to be preserved. Based on our results, the recurrence interval for ruptures along the Maule portion of the subduction zone large enough to be preserved in the stratigraphic record is ~160 years. The recurrence interval between ruptures along the Valdivia portion of the subduction zone at our sites is ~260 years, consistent with a recurrence rate of ~280 years determined by Cisternas et al. (2005) in tidal lowland sections at Maullín and by Moernaut et al. (2014) from lacustrine turbidite stratigraphy east of Valdivia.

4.6. Controls on slip variability at Tirúa and Quidico

Segmentation of subduction zone earthquakes has been attributed to upper-plate (e.g., Audin et al., 2008; Shennan et al., 2009) and lower-plate (e.g., Subarya et al., 2006; Perfettini et al., 2010; Meltzner et al., 2012) structures arresting rupture propagation, although some earthquakes cross such barriers (Nanayama et al., 2003; Taylor et al., 2008; Udías et al., 2012; Briggs et al., 2014). Within the Maule portion of the subduction zone, the only major oceanic feature is the Mocha fracture zone and it is thought to have little influence on rupture propagation (Jara-Munoz et al., 2015). A sharp gradient in petrophysical properties of the upper plate across the Lanalhue fault, which defines the southern limit of the Arauco Peninsula, has been proposed as a barrier to rupture propagation (Melnick et al., 2009), however later studies found no major changes in seismic velocities across the fault, suggesting that other crustal-scale processes control rupture propagation (Haberland et al., 2009).

Jara-Munoz et al. (2015) propose that the long-term rapid uplift

at the Arauco Peninsula, likely controlled by the curvature and the depth of the plate interface, may reflect changes in frictional properties of the megathrust that control slip propagation. This is consistent with the findings of Moreno et al. (2012), who noted that inflections in the curvature of the megathrust correlated with major gradients in coseismic slip at the Arauco Peninsula during the 2010 earthquake, and Lin et al. (2013), who used slip models from the 2010 and 1960 earthquakes to show that the relatively low frictional properties observed below the Arauco Peninsula allowed the ruptures to propagate into but not through the area. Lin et al. (2013) further noted that the observed velocity-strengthening frictional behavior at the Arauco Peninsula was modest, and the barrier effect of the area is likely due to the relatively large size (~100 km) of the velocity-strengthening patch.

Our coseismic land-level change reconstructions at Tirúa and Quidico—in combination with historical accounts of uplift and subsidence north and south of our sites—show that at least seven megathrust ruptures have propagated into, but not through the Arauco Peninsula over the last ~600 years, supporting the persistence of the megathrust rupture boundary. Further, our results suggest that the complex slip patterns observed at the Arauco Peninsula are influenced by the southern or northern genesis of ruptures. Similar to the 2010 earthquake, previous ruptures on the Maule portion of the subduction zone in 1835 and 1751 reached at least ~30 km south of the Lanalhue fault to our sites, with deep, landward slip on the megathrust producing coastal uplift. Historical ruptures on the Valdivia portion of the subduction zone produced subsidence at or near our sites in 1960 AD and 1575, suggesting that shallow to intermediate depth slip extended at least to the latitude of Tirúa and Quidico. However, no evidence of land-level change associated with these ruptures has been reported north of the Arauco Peninsula, suggesting that ruptures on the Valdivia portion of the subduction zone may not propagate as far into the Arauco Peninsula as northern ruptures. Because our observations of prehistoric coseismic uplift in 1470–1570 AD and subsidence in 1425–1455 AD are limited to Tirúa and Quidico, we cannot determine whether or not these ruptures propagated through the Arauco Peninsula.

Our evidence for long-term slip variability at the overlap of the Maule and Valdivia portions of the subduction zone is consistent with previous studies that suggest that the frictional properties of the area influence slip propagation. The repeated propagation of ruptures into, but not through the Arauco Peninsula suggests the area has persisted as a long-term impediment to slip through at least seven of the last megathrust earthquakes (~600 years). However, the variable land-level change associated with these ruptures confirms the long-term complexity of coseismic slip patterns in the area, which should be considered in hazards assessment.

5. Conclusions

We used stratigraphic, lithologic, and diatom analyses and radiocarbon and ^{137}Cs dating to identify eight instances of coseismic land-level change and tsunami inundation between AD ~150 and 2010 at Tirúa and Quidico. Eight widespread anomalous sand beds display physical characteristics and diatom assemblages indicative of a seaward source and high-energy deposition, consistent with tsunami inundation. Diatom analyses reveal coseismic uplift coincident with sand bed deposition during historical ruptures on the Maule portion of the subduction zone in 2010 AD (uplift measured through surveying), 1835, and 1751 and no land-level change or coseismic subsidence during ruptures on the Valdivia portion of the subduction zone in 1960 AD and 1575. We describe previously undocumented evidence of prehistoric coseismic land-level change coincident with sand bed deposition at Tirúa during ruptures in 1520 AD ± 50 (sand bed 6; uplift), 1440 ± 15 (sand bed 7; subsidence), and 340 ± 70 (sand bed 8; possible uplift). Based on historical patterns of coseismic land-level change, we attribute uplift in 1520 AD ± 50 and 340 ± 70 to ruptures on the Maule portion of the subduction zone and subsidence in 1440 ± 15 to ruptures on the Valdivia portion of the subduction zone.

We correlate our evidence of coseismic land-level change and tsunami inundation with other records of historical and prehistoric earthquakes in the region, and infer a slip distribution for both historical and prehistoric ruptures. Using a simple model of variable coseismic slip and vertical displacement, we show that intermediate to shallow, offshore slip on the megathrust (e.g., slip during the 1960 AD Valdivia rupture) will result in no land-level change or coseismic subsidence at our sites, respectively, and deep or wide, landward slip (e.g., slip during the 2010 AD Maule rupture) will result in coseismic uplift. Our results show that complex slip patterns in the Arauco Peninsula area are influenced by the southern or northern genesis of the ruptures; ruptures on the Maule portion of the subduction zone typically cause uplift at our sites, and ruptures on the Valdivia portion of the subduction typically cause subsidence or no land-level change. The variable uplift and subsidence history recorded at Tirúa and Quidico during megathrust ruptures shows that ruptures along the Valdivia and Maule portions of the subduction zone have repeatedly propagated into and overlapped within the Arauco Peninsula, but have not propagated through the peninsula. This suggests that the area has persisted as a long-term impediment to slip through at least seven of the last megathrust earthquakes (~600 years).

Acknowledgments

This work was supported by funding from National Science Foundation awards to TD and BPH (EAR-566253), TD, BPH, and LLE (EAR-1624533), BPH and LLE (EAR-1145170), LLE and RLW (EAR-1036057), National Geographic Society Research Grant 8577-08 to LLE and MC, and Chile Fondo Nacional de Desarrollo Científico y Tecnológico (FONDECYT N° 1150321) and the Millennium Nucleus CYCLO (ICM grant NC160025) to MC. We thank Brian Atwater, Ed Garrett, Marcelo Lagos, Andrew McConkey, Caitlin Orem, and Daniel Ramirez for collaboration in field or laboratory research, and Sonja Hausmann and Don Charles at Academy of Natural Sciences in Philadelphia, USA for their assistance with diatom analyses. Nelson and Wesson are supported by the Earthquake Hazards Program of the U.S. Geological Survey. Any use of trade, product, or firm names is for descriptive purposes only and does not imply endorsement by the U.S. Government. This work is a contribution to IGCP (International Geoscience Programme) Project 639.This work comprises Earth Observatory of Singapore contribution no. 162. This research is supported by the National Research Foundation Singapore and the Singapore Ministry of Education under the Research Centres of Excellence initiative.

Appendix A. Supplementary data

Supplementary data related to this article can be found at https://doi.org/10.1016/j.quascirev.2017.08.023.

References

Allen, J.R.L., 2000. Morphodynamics of holocene salt marshes: a review sketch from the Atlantic and Southern North sea coasts of Europe. Quat. Sci. Rev. 19, 1155–1231.

Angermann, D., Klotz, J., Reigber, C., 1999. Space-geodetic estimation of the Nazca-South America Euler vector. Earth Planet. Sci. Lett. 171, 329–334.

Atwater, B.F., Hemphill-Haley, E., 1997. Recurrence Intervals for Great Earthquakes of the Past 3,500 Years at Northeastern Willapa Bay, vol. 1576. U.S. Geological Survey Professional Paper, Washington, pp. 1–108.

Atwater, B.F., Nunez, H.J., Vita-Finzi, C., 1992. Net late Holocene emergence despite earthquake-induced submergence, South-Central Chile. In: Ota, Y., Nelson, A.R., Berryman, K.R. (Eds.), Impacts of Tectonics on Quaternary Coastal Evolution, 15/16. Quaternary International, Pergamon, Oxford, pp. 77–85.

Audin, L., Lacan, P., Tavera, H., Bondoux, F., 2008. Upper plate deformation and seismic barrier in front of Nazca subduction zone: the Chololo Fault System and active tectonics along the Coastal Cordillera, Southern Peru. Tectonophysics 459 (1), 174–185.

Barrientos, S.E., 2007. Earthquakes in Chile. In: Moreno, T., Gibbons, W. (Eds.), Geology of Chile. The Geological Society, London, pp. 263–287.

Bartsch-Winkler, S., Schmoll, H., 1993. Evidence for late Holocene relative sea-level fall from reconnaissance stratigraphical studies in an area of earthquake-subsided intertidal deposits, Isla Chiloé, Southern Chile. In: Frostwick, L.E., Steel, R.J. (Eds.), Tectonic Controls and Signatures in Sedimentary Successions. International Association of Seismologists, pp. 91–108.

Beck, S., Barrientos, S.E., Kausel, E., Reyes, M., 1998. Source characteristics of historical earthquakes along central Chile subduction zone. J. S. Am. Earth Sci. 11, 115–129.

Bilek, S.L., 2010. Invited review paper: seismicity along the South American subduction zone: review of large earthquakes, tsunamis, and subduction zone complexity. Tectonophysics 495 (1), 2–14.

Birks, H.J.B., 1986. Numerical zonation, comparison and correlation of Quaternary pollen-stratigraphical data. In: Berglund, B.E. (Ed.), Handbook of Holocene Palaeoecology and Palaeohydrology. John Wiley and Sons Ltd, London, pp. 743–773.

Birks, H.J.B., 1992. Some Reflections on the Application of Numerical Methods in Quaternary Palaeoecology, vol. 102. University of Joensuu Publication, Karelian Institute, pp. 7–20.

Bondevik, S., Mangerud, J., Dawson, S., Dawson, A., Lohne, Ø., 2005. Evidence for three North sea tsunamis at the Shetland Islands between 8000 and 1500 years ago. Quat. Sci. Rev. 24 (14), 1757–1775.

Briggs, R.W., Engelhart, S.E., Nelson, A.R., Dura, T., Kemp, A.C., Haeussler, P.J., Corbett, D.R., Angster, S.J., Bradley, L.A., 2014. Uplift and subsidence reveal a non-persistent megathrust rupture boundary (Sitkinak Island, Alaska). Geophys. Res. Lett. 41 (7), 2289–2296.

Bronk Ramsey, C., 2008. Depositional models for chronological records: quaternary science reviews, 27 (1–2), 42–60. https://doi.org/10.1016/j.quascirev.2007.01.019.

Buck, C.E., Cavanagh, W.G., Litton, C.D., 1996. Bayesian Approach to Interpreting Archaeological Data. Book. John Wiley and Sons Ltd, Chichester.

Carvajal, M., Gubler, A., 2016. The effects on tsunami hazard assessment in Chile of assuming earthquake scenarios with spatially uniform slip. Pure Appl. Geophys. 173 (12), 3693–3702.

Carvajal, M., Cisternas, M., Catalan, P.A., 2017. Source of the 1730 Chilean earthquake from historical records: implications for the future tsunami hazard on the coast of Metropolitan Chile. J. Geophys. Res. Solid Earth. https://doi.org/10.1002/2017JB014063.

Cifuentes, I., 1989. The 1960 Chilean earthquakes. J. Geophys. Res. 94, 665–680.

Cisternas, M., Torrejón, F., Gorigoitia, N., 2012. Amending and complicating Chile's seismic catalog with the Santiago earthquake of 7 August 1580. J. S. Am. Earth Sci. 33, 102–109.

Cisternas, M., Araneda, A., Martínez, P., 2001. Effects of historical land use on sediment yield from a lacustrine watershed in Central Chile. Earth Surf. Process. Landforms 26, 63–76.

Cisternas, M., Atwater, B.F., Torrejón, F., Sawai, Y., Machuca, G., Lagos, M., Husni, M., 2005. Predecessors of the giant 1960 Chile earthquake. Nature 437 (7057), 404–407.

Cisternas, M., Garret, E., Wesson, R., Dura, T., Ely, L., 2017a. Unusual geologic evidence for coeval seismic shaking and tsunamis shows variability in earthquake size and recurrence in the area of the giant 1960 Chile earthquake. Mar. Geol. 385, 101–113.

Cisternas, M., Carvajal, M., Wesson, R., Ely, L., Gorigoitia, N., 2017b. Exploring the historical earthquakes preceding the giant 1960 Chile earthquake in a time-dependent seismogenic zone. Bull. Seismol. Soc. Am (in press).

Cochran, U., Hannah, M., Harper, M., Van Dissen, R., Berryman, K., Begg, J., 2007. Detection of Large, Holocene Earthquakes Using Diatom Analysis of Coastal Sedimentary Sequences, Wellington, New Zealand. Quaternary Science Reviews vol. 26 (7), 1129–1147.

Dawson, S., Smith, D.E., Ruffman, A., Shi, S., 1996. The diatom biostratigraphy of tsunami sediments: examples from recent and middle Holocene events. Phys. Chem. Earth 21 (1), 87–92.

Dawson, S., Smith, D.E., 2000. The sedimentology of middle Holocene tsunami facies in Northern Sutherland, Scotland, UK. Mar. Geol. 170 (1–2), 69–79. https://doi.org/10.1016/S0025-3227(00)00066-9.

Darwin, C., 1839. Journal and Remarks. 1832-1836, *in* Narrative of the Surveying Voyages of His Majesty's Ships Adventure and Beagle, between the Years 1826 and 1836, V. III. Henry Colburn (reprinted in 1966 by AMS Press, Inc., New York), London.

Denys, L., 1991. A Check-List of the Diatoms in the Holocene Deposits of the Western Belgian Coastal Plain with a Survey of Their Apparent Ecological Requirements. Ministère des affaires économiques, Service Géologique de Belgique.

de Moralda, J.M., 1780's. Plano de la Bahía de Concepción de Chile.

Dragert, H., Wang, K., James, T.S., 2001. A silent slip event on the deeper Cascadia subduction interface. Science 292 (5521), 1525–1528.

Dura, T., Cisternas, M., Horton, B.P., Ely, L.L., Nelson, A.R., Wesson, R.L., Pilarczyk, J.E., 2015. Coastal evidence for Holocene subduction-zone earthquakes and tsunamis in central Chile. Quat. Sci. Rev. 113, 93–111.

Dura, T., Hemphill-Haley, E., Sawai, Y., Horton, B.P., 2016a. The application of diatoms to reconstruct the history of subduction zone earthquakes and tsunamis. Earth-Science Rev. 152, 181–197.

Dura, T., Engelhart, S.E., Vacchi, M., Horton, B.P., Kopp, R.E., Peltier, W.R., Bradley, S., 2016b. The role of holocene relative sea-level change in preserving records of subduction zone earthquakes. Curr. Clim. Change Rep. 2 (3), 86–100.

Ely, L.L., Webb, R.H., Enzel, Y., 1992. Accuracy of post-bomb 137 Cs and 14 C in dating fluvial deposits. Quat. Res. 38 (2), 196–204.

Ely, L.L., Cisternas, M., Wesson, R., Dura, T., 2014. Five centuries of tsunamis and land-level changes in the overlapping rupture area of the 1960 and 2010 Chilean earthquakes. Geology G35830–G35831. https://doi.org/10.1130/G35830.1.

Farías, M., Vargas, G., Tassara, A., Carretier, S., Baize, S., Melnick, D., Bataille, K., 2010. Land-level changes produced by the M_w 8.8 2010 Chilean earthquake. Science 329, 916.

FitzRoy, R. (Ed.), 1839. Narrative of the Surveying Voyages of His Majesty's Ships Adventure and Beagle, between the Years 1826 and 1836: Describing Their Examination of the Southern Shores of South America, and the Beagle's Circumnavigation of the Globe … H. Colburn.

Garrett, E., Shennan, I., Woodroffe, S.A., Cisternas, M., Hocking, E.P., Gulliver, P., 2015. Reconstructing paleoseismic deformation, 2: 1000 years of great earthquakes at Chucalén, south central Chile. Quat. Sci. Rev. 113, 112–122.

Garrett, E., Shennan, I., Watcham, E.P., Woodroffe, S.A., 2013. Reconstructing paleoseismic deformation, 1: modern analogues from the 1960 and 2010 Chilean great earthquakes. Quat. Sci. Rev. 75 (0), 11–21. https://doi.org/10.1016/j.quascirev.2013.04.007.

Goto, K., Chagué-Goff, C., Fujino, S., Goff, J., Jaffe, B., Nishimura, Y., Richmond, B., Sugawara, D., Szczuciński, W., Tappin, D.R., Witter, R., Yulianto, E., 2011. New insights of tsunami hazard from the 2011 Tohoku-oki event. Mar. Geol. 290, 46–50.

Haberland, C., Rietbrock, A., Lange, D., Bataille, K., Dahm, T., 2009. Structure of the seismogenic zone of the southcentral Chilean margin revealed by local earthquake traveltime tomography. J. Geophys. Res. : Solid Earth 114 (B1).

Hamilton, S., Shennan, I., 2005. Late Holocene relative sea-level changes and the earthquake deformation cycle around upper Cook Inlet, Alaska. Quat. Sci. Rev. 24 (12), 1479–1498.

Hartley, B., Ross, R., Williams, D.M., 1986. A check-list of the freshwater, brackish and marine diatoms of the British Isles and adjoining coastal waters. J. Marine Biol. Assoc. U.K. 66 (03), 531–610.

Hawkes, A.D., Horton, B.P., Nelson, A.R., Vane, C.H., Sawai, Y., 2011. Coastal subsidence in Oregon, USA, during the giant Cascadia earthquake of AD 1700. Quat. Sci. Rev. 30 (3), 364–376.

Hemphill-Haley, E., 1995. Diatom evidence for earthquake-induced subsidence and tsunami 300 years ago in southern coastal Washington. Geol. Soc. Am. Bull. 107, 367–378.

Hemphill-Haley, E., 1996. Diatoms as an aid in identifying late-Holocene tsunami deposits. The Holocene 6 (4), 439–448.

Hogg, A.G., Hua, Q., Blackwell, P.G., Niu, M., Buck, C.E., Guilderson, T.P., Heaton, T.J., 2013. SHCAL13 Southern Hemisphere calibration, 0–50,000 Years CAL BP. Radiocarbon 55 (4).

Hong, I., Dura, T., Ely, L.L., Horton, B.P., Nelson, A.R., Cisternas, M., Nikitina, D., Wesson, R.L., 2017. A 600-year-long stratigraphic record of tsunamis in south-central Chile. The Holocene 27 (1), 39–51.

Horton, B.P., Edwards, R.J., 2006. Quantifying holocene sea level change using intertidal foraminifera: lessons from the British Isles, Cushman foundation for foraminiferal research. Spec. Publ. (40), 97.

Horton, B.P., Sawai, Y., Hawkes, A.D., Witter, R.C., 2011. Sedimentology and paleontology of a tsunami deposit accompanying the great Chilean earthquake of February 2010. Mar. Micropaleontol. 79, 132–138.

Horton, B.P., Milker, Y., Dura, T., Wang, K., Bridgeland, W.T., Brophy, L., Ewald, M., Khan, N.S., Engelhart, S.E., Nelson, A.R., Witter, R.C., 2017. Microfossil measures of rapid sea-level rise: timing of response of two microfossil groups to a sudden tidal-flooding experiment in Cascadia. Geology. G38832–1.

Isla, F.I., Flory, J.Q., Martínez, C., Fernández, A., Jaque, E., 2012. The evolution of the bío bío delta and the coastal plains of the Arauco Gulf, bío bío region: the holocene sea-level Curve of Chile. J. Coast. Res. 28 (1), 102–111.

Jara-Munoz, J., Melnick, D., Brill, D., Strecker, M.R., 2015. Segmentation of the 2010 Maule Chile earthquake rupture from a joint analysis of uplifted marine terraces and seismic-cycle deformation patterns. Quat. Sci. Rev. 113, 171–192.

Kelleher, J.A., 1972. Rupture zones of large South American earthquakes and some predictions. J. Geophys. Res. 77 (11), 2087–2103.

Kemp, A.C., Nelson, A.R., Horton, B.P., 2013. Radiocarbon dating of plant macrofossils from tidal-marsh sediment. In: Shroder, John F. (Ed.), Treatise on Geomorphology, vol. 14. Academic Press, San Diego, pp. 370–388.

Kempf, P., Moernaut, J., Van Daele, M., Vandoorne, W., Pino, M., Urrutia, R., De Batist, M., 2017. Coastal lake sediments reveal 5500 years of tsunami history in south central Chile. Quat. Sci. Rev. 161, 99–116.

Krammer, K., Lange-Bertalot, H., 1986. Bacillarophyceae 2/1. Naviculaceae. In: Ettl, H., Gerloff, J., Heynig, H., Mollenhauser (Eds.), Süsswasserflora von Mitteleuropa. Gustav Fischer Verlag, Stuttgart, pp. 1–876.

Krammer, K., Lange-Bertalot, H., 1988. Bacillariaceae 2/2. Basillariaceae, Epithemiaceae, Surirellaceae. In: Ettl, H., Gerloff, J., Heynig, H., Mollenhauser (Eds.), Süsswasserflora von Mitteleuropa. Gustav Fischer Verlag, Stuttgart, pp. 1–600.
Krammer, K., Lange-Bertalot, H., 1991a. Bacillariaceae 2/3. Centrales, Fragilariaceae, Eunotiaceae. In: Ettl, H., Gerloff, J., Heynig, H., Mollenhauser (Eds.), Süsswasserflora von Mitteleuropa. Gustav Fischer Verlag, Stuttgart, pp. 1–600.
Krammer, K., Lange-Bertalot, H., 1991b. Bacillariaceae 2/4. Achnanthaceae, Kritische Erganzungen zu Navicula (Lineolatae) und Gomphonema. In: Ettl, H. (Ed.), Pascher's Süsswasserflora von Mitteleuropa, vol. 2. Gustav Fischer Verlag, Stuttgart, pp. 1–437 part 4.
Lange-Bertalot, H., 2000. In: Lange-Bertalot, H. (Ed.), Iconographia Diatomologica Annotated Diatom Micrographs – Diatom Flora of Marine Coasts I, Vol. 7. Koeltz Scientific Books. Copyright: A.R.G. Gantner Verlag K.G. By: Andrzej Witkowiski, Horst Lange- Bertalot and Ditmar Metzeltin.
Lay, T., 2011. Earthquakes: a Chilean surprise. Nature 471 (7337), 174–175.
Lomnitz, C., 1970. Major earthquakes and tsunamis in Chile during the period 1535 to 1955. Geologische Rundschau 59 (3), 938–960.
Lin, Y.-n.N., Sladen, A., Ortega-Culaciati, F., Simons, M., Avouac, J.-P., Fielding, E.J., Brooks, B.A., Bevis, M., Genrich, J., Rietbrock, A., Vigny, C., Smalley, R., Socquet, A., 2013. Coseismic and postseismic slip associated with the 2010 Maule Earthquake, Chile: characterizing the Arauco Peninsula Barrier Effect. J. Geophys. Res. Solid Earth 118, 3142e3159.
Lomnitz, C., 2004. Major earthquakes of Chile: a historical survey, 1535-1960. Seismol. Res. Lett. 75 (3), 368–378.
Lorito, S., Romano, F., Atzori, S., Tong, X., Avallone, A., McCloskey, J., Cocco, M., Boschi, E., Piatanesi, A., 2011. Limited overlap between the seismic gap and coseismic slip of the great 2010 Chile earthquake. Nat. Geosci. 4 (3), 173–177.
Melnick, D., Bookhagen, B., Strecker, M.R., Echtler, H.P., 2009. Segmentation of megathrust rupture zones from fore-arc deformation patterns over hundreds to millions of years, Arauco peninsula, Chile. J. Geophys. Res. Solid Earth 114 (B1).
Melnick, D., Cisternas, M., Moreno, M., Norambuena, R., 2012. Estimating coseismic coastal uplift with an intertidal mussel: calibration for the 2010 Maule Chile earthquake (Mw = 8.8). Quat. Sci. Rev. 42, 29–42.
Melnick, D., Moreno, M., Quinteros, J., Baez, J.C., Deng, Z., Li, S., Oncken, O., 2017. The super-interseismic phase of the megathrust earthquake cycle in Chile. Geophys. Res. Lett. 44 (2), 784–791. https://doi.org/10.1002/2016GL071845.
Meltzner, A.J., Sieh, K., Chiang, H.W., Shen, C.C., Suwargadi, B.W., Natawidjaja, D.H., Philibosian, B., Briggs, R.W., 2012. Persistent termini of 2004-and 2005-like ruptures of the Sunda megathrust. J. Geophys. Res. Solid Earth 117 (B4).
Métois, M., Socquet, A., Vigny, C., 2012. Interseismic coupling, segmentation and mechanical behavior of the central Chile subduction zone. J. Geophys. Res. Solid Earth 117 (B3), B03406. https://doi.org/10.1029/2011JB008736.
Moernaut, J., De Batist, M., Charlet, F., Heirman, K., Chapron, E., Pino, M., Brümmer, R., Urrutia, R., 2007. Giant earthquakes in south-central Chile revealed by Holocene mass-wasting events in Lake Puyehue. Sediment. Geol. 195, 239–256.
Moernaut, J., Daele, M.V., Heirman, K., Fontijn, K., Strasser, M., Pino, M., Urrutia, R., De Batist, M., 2014. Lacustrine turbidites as a tool for quantitative earthquake reconstruction: new evidence for a variable rupture mode in South Central Chile. J. Geophys. Res. Solid Earth 119 (3), 1607–1633.
Moreno, M.S., Bolte, J., Klotz, J., Melnick, D., 2009. Impact of megathrust geometry on inversion of coseismic slip from geodetic data: application to the 1960 Chile earthquake. Geophys. Res. Lett. 36 (16), L16310. https://doi.org/10.1029/2009GL039276.
Moreno, M., Melnick, D., Rosenau, M., Bolte, J., Klotz, J., Echtler, H., Baez, J., Bataille, K., Chen, J., Bevis, M., Hase, H., 2011. Heterogeneous plate locking in the South–Central Chile subduction zone: building up the next great earthquake. Earth Planet. Sci. Lett. 305 (3), 413–424.
Moreno, M., Melnick, D., Rosenau, M., et al., 2012. Toward understanding tectonic control on the *Mw* 8.8 2010 Maule Chile earthquake. Earth Planet. Sci. Lett. 321–322, 152–165. https://doi.org/10.1016/j.epsl.2012.01.006.
Munsell soil color charts, 1975. Macbeth Division of Kollmorgen Corporation.
Nanayama, F., Satake, K., Furukawa, R., Shimokawa, K., Atwater, B.F., Shigeno, K., Yamaki, S., 2003. Unusually large earthquakes inferred from tsunami deposits along the Kuril trench. Nature 424 (6949), 660–663.
Nelson, A.R., Shennan, I., Long, A.J., 1996. Identifying coseismic subsidence in tidal-wetland stratigraphic sequences at the Cascadia subduction zone of western North America. J. Geophys. Res. 101, 6115–6135.
Nelson, A.R., Kashima, K., Bradley, L., 2009. Fragmentary evidence of great-earthquake subsidence during Holocene emergence, Valdivia Estuary, South Central Chile. Bull. Seismol. Soc. Am. 99 (1), 71–86.
Nelson, A.R., Briggs, R.W., Dura, T., Engelhart, S.E., Gelfenbaum, G., Bradley, L.A., Forman, S.L., Vane, C.H., Kelley, K.A., 2015. Tsunami recurrence in the eastern Alaska-Aleutian arc: a Holocene stratigraphic record from Chirikof Island, Alaska. Geosphere 11 (4), 1172–1203.
Nentwig, V., Tsukamoto, S., Frechen, M., Bahlburg, H., 2015. Reconstructing the tsunami record in Tirúa, Central Chile beyond the historical record with quartz-based SAR-OSL. Quaternary Geochronol. 30, 299–305.
Peltier, W.R., 2002. On eustatic sea level history: last Glacial Maximum to Holocene. Quat. Sci. Rev. 21 (1), 377–396.
Peltier, W.R., 2004. Global glacial isostasy and the surface of the ice-age Earth: the ICE-5G (VM2) model and GRACE. Annu. Rev. Earth Planet. Sci. 32, 111–149.
Perfettini, H., Avouac, J.P., Tavera, H., Kositsky, A., Nocquet, J.M., Bondoux, F., Chlieh, M., Sladen, A., Audin, L., Farber, D.L., Soler, P., 2010. Seismic and aseismic slip on the Central Peru megathrust. Nature 465 (7294), 78–81.
Pilarczyk, J.E., Dura, T., Horton, B.P., Engelhart, S.E., Kemp, A.C., Sawai, Y., 2014. Microfossils from coastal environments as indicators of paleo-earthquakes, tsunamis and storms. Palaeogeogr. Palaeoclimatol. Palaeoecol. 413, 144–157.
Plafker, G., 1965. Tectonic deformation associated with the 1964 Alaska earthquake. Science 148 (3678), 1675–1687.
Plafker, G., 1972. Alaskan earthquake of 1964 and Chilean earthquake of 1960: implications for arc tectonics. J. Geophys. Res. 77 (5), 901–925.
Plafker, G., Savage, J.C., 1970. Mechanism of the Chilean earthquakes of may 21 and 22, 1960. Geol. Soc. Am. Bull. 81, 1001–1030.
Pollitz, F.F., Bürgmann, R., Banerjee, P., 2006. Post-seismic relaxation following the great 2004 Sumatra-Andaman earthquake on a compressible self-gravitating Earth. Geophys. J. Int. 167 (1), 397–420.
Rebolledo, L., Lange, C.B., Figueroa, D., Pantoja, S., Muñoz, P., Castro, R., 2005. 20th century fluctuations in the abundance of siliceous microorganisms preserved in the sediments of the Puyuhuapi channel (44 S), Chile. Revista Chilena de Historia Natural 78, 469–488.
Rebolledo, L., González, H.E., Muñoz, P., Iriarte, J.L., Lange, C.B., Pantoja, S., Salamanca, M., 2011. Siliceous productivity changes in Gulf of Ancud sediments (42° S, 72° W), southern Chile, over the last~ 150 years. Continental Shelf Res. 31 (3), 356–365.
Rehak, K., Strecker, M.R., Echtler, H.P., 2008. Morphotectonic segmentation of an active forearc, 37-41_ S, Chile. Geomorphology 94, 98–116.
Reid, H.F., 1910. The California Earthquake of April 18, 1906, the Mechanics of the Earthquake. Report 2, State Earthquake Invest. Comm.. Carnegie Institute, Washington, DC.
Rivera, R., 2000. Guide for References and Distribution for the Class Bacillariophyceae in Chile Between 18°28'S and 58°S. J. Cramer.
Roy, K., Peltier, W.R., 2015. Glacial isostatic adjustment, relative sea level history and mantle viscosity: reconciling relative sea level model predictions for the US East coast with geological constraints. Geophys. J. Int. 201 (2), 1156–1181.
Satake, K., Atwater, B.F., 2007. Long-term perspectives on giant earthquakes and tsunamis at subduction zones. Annu. Rev. Earth Planet. Sci. 35, 349–374.
Sawai, Y., 2001. Episodic emergence in the past 3000 years at the Akkeshi Estuary, Hokkaido, northern Japan. Quat. Res. 56, 231–241.
Sawai, Y., Satake, K., Takanobu, K., Nasu, H., Shishikura, M., Atwater, B.F., Horton, B.P., Kelsey, H.M., Nagumo, T., Yamaguchi, M., 2004. Transient uplift after a 17th-century earthquake along the Kuril subduction zone. Science 306, 1918–1920. https://doi.org/10.1126/science.1104895.
Sawai, Y., Fujii, Y., Fujiwara, O., Kamataki, T., Komatsubara, J., Okamura, Y., et al., 2008. Marine incursions of the past 1500 years and evidence of tsunamis at Suijin-numa, a coastal lake facing the Japan Trench. The Holocene 18 (4), 517–528.
Sawai, Y., Jankaew, K., Martin, M.E., Prendergast, A., Choowong, M., Charoentitirat, T., 2009. Diatom assemblages in tsunami deposits associated with the 2004 Indian ocean tsunami at Phra Thong Island, Thailand. Mar. Micropaleontol. 73, 70–79.
Sawai, Y., Namegaya, Y., Okamura, Y., Satake, K., Shishikura, M., 2012. Challenges of anticipating the 2011 Tohoku earthquake and tsunami using coastal geology. Geophys. Res. Lett. 39 (21).
Segall, Paul, 2010. Earthquake and Volcano Deformation. Princeton University Press, Princeton, New Jersey.
Shennan, I., Hamilton, S., 2006. Coseismic and pre-seismic subsidence associated with great earthquakes in Alaska. Quat. Sci. Rev. 25 (1), 1–8.
Shennan, I., Bruhn, R., Plafker, G., 2009. Multi-segment earthquakes and tsunami potential of the Aleutian megathrust. Quat. Sci. Rev. 28 (1), 7–13.
Shennan, I., Bruhn, R., Barlow, N., Good, K., Hocking, E., 2014. Late Holocene great earthquakes in the eastern part of the Aleutian megathrust. Quat. Sci. Rev. 84, 86–97.
Shennan, I., Garrett, E., Barlow, N., 2016. Detection limits of tidal-wetland sequences to identify variable rupture modes of megathrust earthquakes. Quat. Sci. Rev. 150, 1–30.
Sieh, K., Natawidjaja, D.H., Meltzner, A.J., Shen, C., Cheng, H., Li, K., Suwargadi, B.W., Galetzka, J., Philibosian, B., Edwards, R.L., 2008. Earthquake supercycles inferred from sea-level changes recorded in the corals of west Sumatra. Science 322 (5908), 1674–1678.
Simons, M., Minson, S.E., Sladen, A., Ortega, F., Jiang, J., Owen, S.E., Meng, L., Ampuero, J.P., Wei, S., Chu, R., Helmberger, D.V., 2011. The 2011 magnitude 9.0 Tohoku-Oki earthquake: mosaicking the megathrust from seconds to centuries. Science 332 (6036), 1421–1425.
Smith, D.E., Shi, S., Cullingford, R.A., Dawson, A.G., Dawson, S., Firth, C.R., Foster, I.D.L., Fretwell, P., Haggart, B.A., Holloway, L.K., Long, D., 2004. The Holocene Storegga Slide tsunami in the United Kingdom. Quat. Sci. Rev. 23/24, 2291–2321.
Subarya, C., Chlieh, M., Prawirodirdjo, L., Avouac, J.P., Bock, Y., Sieh, K., Meltzner, A.J., Natawidjaja, D.H., McCaffrey, R., 2006. Plate-boundary deformation associated with the great Sumatra–Andaman earthquake. Nature 440 (7080), 46–51.
Szczuciński, W., Kokociński, M., Rzeszewski, M., Chagué-Goff, C., Cachão, M., Goto, K., Sugawara, D., 2012. Sediment sources and sedimentation processes of 2011 Tohoku-oki tsunami deposits on the Sendai Plain, Japan — insights from diatoms, nannoliths and grain size distribution. Sediment. Geol. 282, 40–56. https://doi.org/10.1016/j.sedgeo.2012.07.019.
Taylor, F.W., Briggs, R.W., Frohlich, C., Brown, A., Hornbach, M., Papabatu, A.K., Meltzner, A.J., Billy, D., 2008. Rupture across arc segment and plate boundaries in the 1 April 2007 Solomons earthquake. Nat. Geosci. 1 (4), 253–257.
Thatcher, W., 1990. Order and diversity in the modes of circum-pacific earthquake

recurrence. J. Geophys. Res. Solid Earth 95 (B3), 2609–2623.
Udías, A., Madariaga, R., Buforn, E., Muñoz, D., Ros, M., 2012. The large Chilean historical earthquakes of 1647, 1657, 1730, and 1751 from contemporary documents. Bull. Seismol. Soc. Am. 102 (4), 1639–1653. https://doi.org/10.1785/0120110289.
Vigny, C., Socquet, A., Peyrat, S., Ruegg, J.-C., Métois, M., Madariaga, R., Morvan, S., 2011. The 2010 Mw 8.8 Maule megathrust earthquake of central Chile, monitored by GPS. Science 332 (6036), 1417–1421. https://doi.org/10.1126/science.1204132.
Vos, P.C., Wolf, H.D., 2007. Methodological aspects of paleo-ecological diatom research in coastal areas of the Netherlands. Neth. J. Geosciences/Geologie en Mijnbouw (Classic Papers).
Vos, Peter C., de Wolf, H., 1993. Diatoms as a tool for reconstructing sedimentary environments in coastal wetlands; methodological aspects. In: Twelfth International Diatom Symposium. Springer Netherlands, pp. 285–296.
Wang, K., 2007. Elastic and Viscoelastic Models of Crustal Deformation in Subduction Earthquake Cycles. The Seismogenic Zone of Subduction Thrust Faults, pp. 540–575.
Wang, K., Wells, R., Mazzotti, S., Hyndman, R.D., Sagiya, T., 2003. A revised dislocation model of interseismic deformation of the Cascadia subduction zone. J. Geophys. Res. Solid Earth 108 (B1).
Wang, K., Hu, Y., He, J., 2012. Deformation cycles of subduction earthquakes in a viscoelastic Earth. Nature 484 (7394), 327–332.
Wang, P.L., Engelhart, S.E., Wang, K., Hawkes, A.D., Horton, B.P., Nelson, A.R., Witter, R.C., 2013. Heterogeneous rupture in the great Cascadia earthquake of 1700 inferred from coastal subsidence estimates. J. Geophys. Res. Solid Earth 118 (5), 2460–2473.
Wesson, R.L., Melnick, D., Cisternas, M., Moreno, M., Ely, L.L., 2015. Vertical deformation through a complete seismic cycle at Isla Santa Maria, Chile. Nat. Geosci. 8 (7), 547–551.
Witter, R.C., Kelsey, H.M., Hemphill-Haley, E., 2001. Pacific storms, El Nino and tsunamis: competing mechanisms for sand deposition in a coastal marsh, Euchre Creek, Oregon. J. Coast. Res. 563–583.
Witter, R.C., Kelsey, H.M., Hemphill-Haley, E., 2003. Great Cascadia earthquakes and tsunamis of the past 6700 years, Coquille River estuary, Southern Coastal Oregon. Geol. Soc. Am. Bull. 115 (10), 1289–1306.
Witter, R.C., Briggs, R.W., Engelhart, S.E., Gelfenbaum, G., Koehler, R.D., Barnhart, W.D., 2014. Little late Holocene strain accumulation and release on the Aleutian megathrust below the Shumagin Islands, Alaska. Geophys. Res. Lett. 41 (7), 2359–2367.